

Article

The THDMa Revisited

Tania Robens 

Division of Theoretical Physics, Ruder Boskovic Institute, 10002 Zagreb, Croatia; trobens@irb.hr

Abstract: The THDMa is a new physics model that extends the scalar sector of the Standard Model by an additional doublet as well as a pseudoscalar singlet and allows for mixing between all possible scalar states. In the gauge-eigenbasis, the additional pseudoscalar serves as a portal to the dark sector, with a priori any dark matter spins states. The option where dark matter is fermionic is currently one of the standard benchmarks for the experimental collaborations, and several searches at the LHC constrain the corresponding parameter space. However, most current studies constrain regions in parameter space by setting all but 2 of the 12 free parameters to fixed values. In this work, we performed a generic scan on this model, allowing all parameters to float. We applied all current theoretical and experimental constraints, including bounds from current searches, recent results from B-physics, in particular $B_s \rightarrow X_s \gamma$, as well as bounds from astroparticle physics. We identify regions in the parameter space which are still allowed after these were applied and which might be interesting for an investigation of current and future collider machines.

Keywords: new physics models; collider phenomenology; extended scalar sectors



Citation: Robens, T. The THDMa Revisited. *Symmetry* **2021**, *13*, 2341. <https://doi.org/10.3390/sym13122341>

Academic Editors: Arnaud Ferrari and Jan Kieseler

Received: 31 October 2021
Accepted: 30 November 2021
Published: 6 December 2021

Publisher's Note: MDPI stays neutral with regard to jurisdictional claims in published maps and institutional affiliations.



Copyright: © 2021 by the author. Licensee MDPI, Basel, Switzerland. This article is an open access article distributed under the terms and conditions of the Creative Commons Attribution (CC BY) license (<https://creativecommons.org/licenses/by/4.0/>).

1. Introduction

After the discovery of a scalar boson that complies with predictions of the Standard Model (SM) Higgs boson by the LHC experiments, the quest for additional particles that stem from possible further extensions of the SM scalar sector is an important task for the experimental collaborations. Furthermore, astroparticle observations provide evidence of the existence of dark matter. In a standard cosmological description, the particle content of the SM alone does not suffice to explain these observations. Therefore, many beyond SM (BSM) extensions provide an additional dark matter candidates.

In this work, we concentrated on the model which has been proposed in [1–5]. It extends the scalar sector of the Standard Model by an additional doublet as well as a pseudoscalar singlet, which in turn couples to a fermionic dark matter candidate. The model therefore extends the scalar sector by five additional particles, which we label H, A, a, H^\pm in the mass eigenbasis, as well as a fermionic dark matter candidate χ . In the form discussed here, the model contains 14 free parameters after electroweak symmetry breaking, among which two are fixed by the measurement of the 125 GeV scalar as well as electroweak precision measurements. Furthermore, the models' parameter space is subject to a large number of theoretical and experimental constraints which we will discuss in detail below. Reference [6] contains a detailed discussion as well as benchmark recommendations for the LHC experimental collaborations; these can also be seen in refs [7–15] which performed more recent work on this model. Finally, refs [16–34] report on the experimental constraints of current collider searches on the parameter space in specific parameter regions. Projections for the HL-LHC sensitivity can be found in [35–38].

This manuscript is organized as follows. In Section 2, we briefly review the setup of the model, including the introduction of the conventions used in this work. In Section 3, we discuss the current theoretical and experimental bounds that need to be imposed. Section 4 introduces the setup of our scan and identifies regions in the parameter space that are still allowed after all constraints are taken into account. We present a first glance at possible processes at e^+e^- colliders in Section 5, and conclude in Section 6.

2. The Model

The model discussed in this work was introduced in the references [1–5], and we refer the reader to these works for a detailed discussion of the model setup. We here only list the generic features for brevity. We largely follow the nomenclature of [6].

The field content of the THDMa in the gauge eigenbasis consists of two scalar fields $H_{1,2}$ which transform into doublets under the $SU(2) \times U(1)$ gauge group, and additional pseudoscalar P transforms into a singlet, as well as a dark matter candidate χ which we choose to be fermionic. The two Higgs doublet model (THDM) part of the potential is given by

$$V_{\text{THDM}} = \mu_1 H_1^\dagger H_1 + \mu_2 H_2^\dagger H_2 + \lambda_1 (H_1^\dagger H_1)^2 + \lambda_2 (H_2^\dagger H_2)^2 + \lambda_3 (H_1^\dagger H_1)(H_2^\dagger H_2) \quad (1)$$

$$+ \lambda_4 (H_1^\dagger H_2)(H_2^\dagger H_1) + [\mu_3 H_1^\dagger H_2 + \lambda_5 (H_1^\dagger H_2)^2 + h.c.] \quad (2)$$

Fields are decomposed according to (see also, e.g., [39]):

$$H_i = \begin{pmatrix} \phi_i \\ \frac{1}{\sqrt{2}}(v_i + \rho_i + i\eta_i) \end{pmatrix} \quad (3)$$

where:

$$v_1 = v \cos \beta, \quad v_2 = v \sin \beta. \quad (4)$$

The scalar potential is:

$$V_P = \frac{1}{2} m_P^2 P^2 + \lambda_{P_1} H_1^\dagger H_1 P^2 + \lambda_{P_2} H_2^\dagger H_2 P^2 + (i b_P H_1^\dagger H_2 P + h.c.). \quad (5)$$

Finally, the coupling between the visible and the dark sector is mediated via the interaction:

$$\mathcal{L}_\chi = -i y_\chi P \bar{\chi} \gamma_5 \chi.$$

Couplings of the scalar sector to the fermionic sector are equivalent to a THDM type II (see, e.g., [39]) and follow from:

$$\mathcal{L}_Y = - \sum_{i=1,2} \left\{ \bar{Q} Y_u^i \tilde{H}_i u_R + \bar{Q} Y_d^i H_i d_R + \bar{L} Y_\ell^i H_i \ell_R + h.c. \right\},$$

where $Y_{u,d}^i$ denote the Yukawa matrices, Q and L are the left-handed quark and lepton doublets, u_R, d_R, ℓ_R label right-handed up-type, down-type, and leptonic singlets, and $\tilde{H} = \epsilon H_i^*$, where $\epsilon = i\sigma_2$ denotes the two-dimensional antisymmetric tensor. We impose an additional Z_2 symmetry on the model, under which the doublets transform into $H_1 \rightarrow H_1, H_2 \rightarrow -H_2$ in order to avoid contributions from flavor-changing neutral currents. We further set the transformation properties of the additional fields to $P \rightarrow P, \chi \rightarrow -\chi$. In this work, we concentrated on the case where $Y_1^u = Y_2^d = Y_2^\ell = 0$, which corresponds to a type II classification of Yukawa couplings in the THDM notation and can be achieved by requiring $u_R \rightarrow -u_R$ under the said symmetry. Note that the terms $\sim \mu_3, b_P$ induce a soft Z_2 breaking.

After electroweak symmetry breaking, the model is characterized by a total of 14 free parameters. The above potential induces standard mixing for the THDM part of the potential, which we characterize by $\cos(\beta - \alpha)$, $\tan \beta$ using standard notation. Furthermore, V_P introduces a mixing between the pseudoscalar part of the THDM and the new pseudoscalar P , with physical states given by

$$\begin{pmatrix} a \\ A \end{pmatrix} = \begin{pmatrix} c_\theta & -s_\theta \\ s_\theta & c_\theta \end{pmatrix} \begin{pmatrix} P \\ A^0 \end{pmatrix}$$

where we use the notation $c_x \equiv \cos x$, $s_x \equiv \sin x$ here and in the following and A^0 denotes the mass-eigenstate of the pseudoscalar from V_{THDM} prior to mixing. We choose as free parameters:

$$v, m_h, m_A, m_H, m_{H^\pm}, m_a, m_\chi, \cos(\beta - \alpha), \tan \beta, \sin \theta, y_\chi, \lambda_3, \lambda_{P_1}, \lambda_{P_2} \quad (6)$$

following the suggestions in [6]. The relations between these and other quantities in the Lagrangian can be found in Appendix A.

For the parameters in Equation (6), v and m_h are fixed to ~ 246 GeV and ~ 125 GeV, respectively. In principle, one can also consider the case that $m_H \sim 125$ GeV, with m_h being a lighter resonance, though we discard this scenario in the following. We are therefore left with 12 parameters which can a priori vary, but are obviously subject to theoretical and experimental constraints. Previous studies of this model usually chose to consider scenarios where all but a few are fixed, in order to facilitate the phenomenological exploration and provide consistent benchmark scenarios for comparison. In this work, we allow all parameters to float and determine regions in the models' parameter space that are highly populated. Fine-tuned regions might exist within this model which are missed in a generic scan setup.

3. Theoretical and Experimental Constraints

The models' parameter space is subject to a list of theoretical and experimental constraints which we list below.

3.1. Perturbativity, Perturbative Unitarity and Positivity of the Potential

In order to guarantee the positivity of the potential, several relations between the potential parameters need to be obeyed (as can be seen, e.g., in [6,12,14]). In the notation introduced here, they are given by

$$\lambda_{1,2,P_1,P_2} \geq 0, \lambda_3 \geq -2\sqrt{\lambda_1 \lambda_2}, \lambda_3 + \lambda_4 - 2|\lambda_5| \geq -2\sqrt{\lambda_1 \lambda_2}.$$

Furthermore, we require the self-couplings in the potential to obey an upper limit, which we chose as 4π . We therefore have:

$$|\lambda_i| \leq 4\pi, \left| \frac{b_P}{v} \right| \leq 4\pi.$$

Finally, bounds from perturbative unitarity were implemented using the perturbative unitarity bounds derived in [12]; we refer the reader to that work for more details as well as explicit analytic expressions. We furthermore check that Equation (3.11) of [14]. (taken from [3]) is fulfilled.

3.2. Constraints from Electroweak Precision Observables, Flavor Constraints, and Total Widths

These bounds are tested via an implementation in SPheno [40,41], using an interface with Sarah [42–46]. Constraints from the measurements of electroweak precision observables are taken into account using the oblique parameters S, T, U [47–49] as parametrization. We take the latest fit results from the Gfitter collaboration [50–52], with central values given by

$$S = 0.04 \pm 0.11, T = 0.09 \pm 0.14, U = -0.02 \pm 0.11$$

and the correlation matrix as given in the above references. We demand that $\Delta\chi^2 \leq 8.02489$, which corresponds to a 2σ region around the central value determined by the SM decoupling.

Two Higgs doublet models and their extensions are also subject to strong bounds from flavor constraints, cf. e.g., [52,53]. The $m_{H^\pm}, \tan \beta$ plane is especially strongly constrained by precision flavor observables as, e.g., $B \rightarrow X_s \gamma$, $B_s \rightarrow \mu^+ \mu^-$, and ΔM_s . For these variables, we consider the following allowed regions:

- $B \rightarrow X_s \gamma$
The most recent results of the theoretical calculation of this variable including higher order calculations up to NNLO in QCD were presented in [54], superseding previous results [55]. In particular, the charged scalar mass is pushed to even higher masses. We implement the lower bound in this variable using a two-dimensional fit function [56] that reflects the bounds derived in [54].
- $B_s \rightarrow \mu^+ \mu^-$
The ATLAS, CMS and LHCb combination using 2011–2016 LHC data for the branching ratio $B_s \rightarrow \mu^+ \mu^-$ is given by [57]

$$(B_s \rightarrow \mu^+ \mu^-)^{\text{comb}} = [2.69_{-0.35}^{+0.37}] \times 10^{-9}. \quad (7)$$

In principle, theoretical predictions depend on all novel scalar masses (see, e.g., [58]). In the decoupling limit, Spheno renders the SM output:

$$B_s \rightarrow \mu^+ \mu^- = 2.96 \times 10^{-9},$$

while the most recent theoretical calculation yields [59]:

$$B_s \rightarrow \mu^+ \mu^- = (3.66 \pm 0.14) \times 10^{-9}.$$

Note that this disagrees with the experimental result (Equation (7)) by 2.5σ .

In order to account for the missing higher-order corrections, we apply a multiplicative correction factor to the Spheno result.

Again assuming a similar error in the theory calculation, and taking into account the additional higher-order shift to the Spheno result, we then have:

$$(B_s \rightarrow \mu^+ \mu^-)^{\text{Spheno}} \in [1.26; 3.14] \times 10^{-9},$$

where we allow for a 3σ deviation.

- ΔM_s
The most recent experimental result for this value is given by $\Delta M_s (\text{ps}^{-1}) = 17.757 \pm 0.020 \pm 0.007$ [60].
We use the following derivation for the SM prediction for this value: We start with Equation (31) of [61]:

$$\Delta M_s = 17.24 \text{ps}^{-1} \left(\frac{|V_{tb} V_{ts}^*|}{0.04} \right)^2 \frac{S(\bar{m}_t^2/m_W^2)}{2.35} \frac{f_{B_s}^2 \mathcal{B}_{B_s}}{(0.21 \text{GeV})^2} |\Delta_s|$$

which shows the dependency of this variable on external, experimentally determined parameters. The above expression was updated to [62,63]:

$$\Delta M_s = 17.3 \text{ps}^{-1} \frac{f_{B_s}^2 \mathcal{B}_{B_s}}{(211.84 \text{MeV})^2} \frac{|V_{cb}|^2}{0.04089^2}.$$

For input values [64–66]:

$$f_{B_s} = (230.3 \pm 1.3) \text{MeV}, \hat{\mathcal{B}}_{B_s} = 1.232 \pm 0.053, V_{cb} = (42.2 \pm 0.8) \times 10^{-3},$$

together with the conversion factor $\hat{\mathcal{B}}_{B_s} = 1.52319 \mathcal{B}_{B_s}$ [62], we then obtain:

$$\Delta M_s = (17.61 \pm 1.05) \text{ps}^{-1},$$

where we furthermore assumed an intrinsic error of 0.2 on the central value [63], which mainly stems from uncertainties of the top mass (neglecting this leads to a slightly smaller error of $\pm 1.03 \text{ps}^{-1}$).

The SpHeno decoupling result is given by $(\Delta M_s)^{\text{SpHeno}} = 18.801 \text{ ps}^{-1}$.

Assuming the new physics contributions to be multiplicative, while keeping the error additive (T.R. gratefully acknowledges M. Mikolaj for useful discussions regarding this point), we then have:

$$\left[\Delta M_s (\text{ps}^{-1}) \right]^{\text{SpHeno}} \in [16.71; 21.19] \text{ ps}^{-1} \quad (8)$$

as an allowed 2σ range for this value.

Finally, although not strictly required, we impose an upper bound on the width over the mass ratio on all new scalars. For the 125 GeV candidate, we require that [67]:

$$\Gamma_{h,125} \leq 9 \text{ MeV}. \quad (9)$$

For all other scalars, we impose

$$\Gamma/M \leq 0.5. \quad (10)$$

We consider this a very lenient bound in order to allow a detailed investigation of the parameter space; in practice, ratios larger than 10–20% already strongly question the applicability of perturbative treatment for such states.

3.3. Collider Bounds

Agreement with current measurements of the 125 GeV signal strength as well as agreement with null-results from a large number of searches were tested by interfacing the model with HiggsBounds [68–74] and HiggsSignals [73,75–78]. Furthermore, the model is additionally constrained by dedicated searches by the LHC experiments; we implemented the corresponding bounds in a pseudo-approximate approach and leave a detailed recast analysis for future work. All production cross-sections were produced using Madgraph5 [79], with the UFO model provided in [4,80]:

- **Bounds from $\ell^+\ell^- + \text{MET}$ searches**

We consider the experimental bounds presented in [22] which correspond to a CMS search for this channel mediated via Za production using full Run 2 luminosity. For the parameters specified in figure 8 in that work, we generate parton-level events. In order to marginally mimic the experimental cuts, we imposed:

$$p_{\perp,\ell} > 25 \text{ GeV}, \quad \cancel{E}_{\perp} > 80 \text{ GeV}, \quad m_{\ell\ell} \in [76, 106] \text{ GeV}, \\ p_{\perp}^{\ell\ell} > 60 \text{ GeV}, \quad |\eta_{\ell}| \leq 2.4, \quad \Delta R_{\ell\ell} \leq 1.8$$

at the parton-level. Results for two specific parameter points using the above cuts are given in Table 1.

Table 1. Results for parton-level generation with rudimentary cuts for points which are excluded by $\ell^+\ell^- + \cancel{E}_{\perp}$ searches in [22]. Other values are set to $m_H = m_{H^{\pm}} = m_A$, $m_{\chi} = 10 \text{ GeV}$, $\cos(\beta - \alpha) = 0$, $\lambda_3 = \lambda_{P_1} = \lambda_{P_2} = 3$, $y_{\chi} = 1$.

m_a	m_A	$\sin \theta$	$\tan \beta$	$\sigma (\text{pb})$
220 GeV	400 GeV	0.35	1	0.01066 (3)
320 GeV	650 GeV	0.35	1	0.00332 (3)
420 GeV	1000 GeV	0.35	1	0.0007296 (9)

A first estimate for sensitivity regions would therefore be to only allow parameter points with:

$$\sigma \leq 0.0007314 \text{ pb}, \quad (11)$$

and simulating all parameter points using the cuts specified above. However, this is especially computationally intensive. Therefore, it is useful to consider the main channel leading to the above signature which is:

$$pp \rightarrow H \rightarrow aZ$$

with subsequent decays $a \rightarrow \chi\bar{\chi}$, $Z \rightarrow \ell^+\ell^-$. The value from factorized onshell production times the decay branching ratios in the $Z\chi\bar{\chi}$ final state for the above benchmark points is given in Table 2.

Table 2. Parameter points in Table 1, relevant quantities. Last column is derived from previous entries.

m_a	m_A	m_H	σ_H (pb)	$H \rightarrow aZ$	$a \rightarrow \chi\bar{\chi}$	$\sigma_{Z\chi\bar{\chi}}^{\text{fac}}$ (pb)
220 GeV	400 GeV	400 GeV	3.70 (1)	0.11	1	0.407 (1)
320 GeV	650 GeV	650 GeV	0.534 (1)	0.13	1	0.0694 (1)
420 GeV	1000 GeV	1000 GeV	0.0497 (2)	0.28	0.86	0.01197 (5)

We could therefore use as a naive condition that:

$$\sigma_{Z\chi\bar{\chi}}^{\text{fac}} \equiv \sigma_{pp \rightarrow H} \times \text{BR}_{H \rightarrow Za} \times \text{BR}_{a \rightarrow \chi\bar{\chi}} \leq 0.01207. \quad (12)$$

A more thorough inspection shows that the above bound has to be modified to:

$$\sigma_{Z\chi\bar{\chi}}^{\text{fac}} \leq 0.009085 \text{ pb}$$

in order to capture all points from our scan which obey Equation (11).

- **Bounds from $h + \text{MET}$ searches**

The above channel for this model has been investigated in [31,32] by the ATLAS collaboration using the full Run 2 dataset. We found that results for the $b\bar{b}$ decay of the h [32] supersede those of the $\gamma\gamma$ decay [31] and therefore concentrate on the former in the following. Note that the search was separated into a resolved and an unresolved region; for the resolved, we require $E_{\perp} > 500$ GeV, while for the unresolved, we have $E_{\perp} \in [150; 500]$ GeV, $p_{\perp,h} > 100$ GeV. We show the values using these cuts for some sample points in Table 3.

Table 3. Results for parton-level generation with rudimentary cuts for points which are excluded by $h + E_{\perp}$ searches in [32]. Other values are set to $m_H = m_{H^{\pm}} = m_A$, $m_{\chi} = 10$ GeV, $\cos(\beta - \alpha) = 0$, $\lambda_3 = \lambda_{p_1} = \lambda_{p_2} = 3$, $y_{\chi} = 1$, $\sin\theta = 0.35$, $\tan\beta = 1$. $\sigma_{\text{res/unres}}$ refers to the resolved/unresolved region as discussed in the text.

m_a	m_A	σ_{res} (pb)	σ_{unres} (pb)
640 GeV	1350 GeV	0.001898 (2)	0.0003709 (5)
300 GeV	500 GeV	0.00493 (2)	$6.79(1) \times 10^{-7}$
180 GeV	1800 GeV	0.00994 (8)	0.0005817 (2)

A priori, the dominant production times decay stems from:

$$pp \rightarrow A \rightarrow ha \rightarrow h\chi\bar{\chi}, \quad (13)$$

where additional contributions can come from:

$$pp \rightarrow A(a) \rightarrow hA(a) \rightarrow h\chi\bar{\chi}, \quad (14)$$

i.e., non-resonant production of $A(a)$ and subsequent decays.

From Table 4, we see that we can roughly exclude points for which the conditions:

$$\sigma_{h+E_{\perp},\text{res}} \leq 0.002818 \text{ pb}, \quad \sigma_{h+E_{\perp},\text{unres}} \leq 6.81 \times 10^{-7} \text{ pb} \quad (15)$$

are not fulfilled. We again want to emphasize that this only corresponds to a very rough sensitivity estimate - particular different regions of the parameter space can be more sensitive to the resolved/unresolved region.

Table 4. Results for parton-level generation with rudimentary cuts for points which are excluded by $h + E_{\perp}$ searches in [32]. Other values are set to $m_H = m_{H^{\pm}} = m_A, m_{\chi} = 10 \text{ GeV}, \cos(\beta - \alpha) = 0, \lambda_3 = \lambda_{P_1} = \lambda_{P_2} = 3, y_{\chi} = 1, \sin\theta = 0.35, \tan\beta = 1$. $\sigma_{\text{res/unres}}$ refers to the resolved/unresolved region as discussed in the text.

m_a	m_A	$\sigma_{\text{res}} \text{ (pb)}$	$\sigma_{\text{unres}} \text{ (pb)}$
500 GeV	1200 GeV	0.00466 (1)	0.000357 (1)
180 GeV	1550 GeV	0.002816 (1)	0.001366 (2)
300 GeV	500 GeV	0.00493 (2)	$6.79 (1) \times 10^{-7}$

For the two points giving the bounds in Equation (15), we have in a factorized approach:

$$\begin{aligned}\sigma_{180,1550}^{\text{fac}} &= \sigma_A \times \text{BR}_{A \rightarrow ha} \times \text{BR}_{a \rightarrow \chi \bar{\chi}} = 0.001728(2) \text{ pb}, \\ \sigma_{300,500}^{\text{fac}} &= \sigma_A \times \text{BR}_{A \rightarrow ha} \times \text{BR}_{a \rightarrow \chi \bar{\chi}} = 0.1158(1) \text{ pb}.\end{aligned}$$

A more detailed investigation shows that for the first parameter point, (13) provides approximately 62% of the cross-section in the resolved region, while for the second, the processes in (14) mainly contribute. In the following, we require that:

$$\sigma_{\text{fac}} = \sigma_A \times \text{BR}_{A \rightarrow ah} \times \text{BR}_{a \chi \bar{\chi}} \leq 0.001732 \text{ pb}.$$

For our sample points, we explicitly checked that this value cuts out all parts of the parameter space where $\sigma_{h+E_{\perp}} \geq 0.002818 \text{ pb}$.

- **Bounds from $H^+ \bar{t}b, H^+ \rightarrow t \bar{b}$ searches**

Searches for the THDM sector of the model can be constrained by the above process, which has been presented, e.g., by the ATLAS collaboration [25] using an integrated luminosity of 139 fb^{-1} , which we compare to the upper bound on the cross-section as available from Hepdata [81]. Even a comparison with the production cross-section for the process:

$$pp \rightarrow H^+ \bar{t}b$$

prior to the charged scalars decay shows that this search is not yet sensitive in the parameter space investigated here. This is mainly caused by the lower limit on $\tan\beta$ from $B \rightarrow X_s \gamma$ which preselects the point with higher $\tan\beta$ values.

- **Bounds from $Wt + \text{MET}$ searches**

The ATLAS collaboration has presented results for this model in the above channel using full Run2 data [23]. They give results for bounds derived from single and double top production, divided into several search regions. We here implemented their results into grid-like upper bounds on the total production cross-section from single-top-like processes, with values taken from Figure 28 of the auxiliary material available from [82]. In the mass region considered here, the smallest upper bound is approximately 32 fb. Note that including $t \bar{t}$ results will improve these bounds. However, here, theoretical cross-sections which were, e.g., used in Figure 31 of the above auxiliary material include the detector simulation and cuts (we thank the authors of the above reference for useful discussions regarding this point.). Including these would require a recast-type investigation, which is beyond the scope of the current work.

- **Bounds from $t \bar{t}/b \bar{b} + \text{MET}$ final states**

The $t \bar{t}$ final states have been investigated in [26,28] using full Run 2 data. We note that a different model file was used for the simulation for the signal, and cross-

sections were rescaled to NLO predictions [83]. In the comparison here, we stick to the leading order, as the QCD higher-order corrections are universal for both models, only differing in the electroweak sector, as long a dominant production is assumed via an s-channel mediator. In Table 5, we give our predictions for the theory cross-section predictions shown in Figure 15 of that reference. Note that for generation, we used $\sin \theta = 1/\sqrt{2}$, as otherwise no significant coupling to both the SM and the dark sector can be achieved. The values in Table 5 were rescaled accordingly (the coupling of a to $t\bar{t}$ is rescaled by $\sin \theta$, while the coupling to $\chi\bar{\chi}$ is rescaled by $\cos \theta$; therefore, in comparison to the calculating in [26] for $g = 1$, we obtain an additional factor $\frac{1}{4}$ in the results). We use $E_{\perp} > 230$ GeV.

Table 5. Results for the parton-level generation with rudimentary cuts for points which are excluded by $t\bar{t} + E_{\perp}$ searches in [26] via a mediation. Other values are set to $m_H = m_A = m_{H^{\pm}} = 600$ GeV, $m_{\chi} = 1$ GeV, $\cos(\beta - \alpha) = 0$, $\lambda_3 = \lambda_{P_1} = \lambda_{P_2} = 3$, $y_{\chi} = 1$, $\tan \beta = 1$. The factor corresponds to a rough estimate of the multiplicative factor from Figure 15 of that reference. The last column gives the actual exclusion cross-section.

m_a (GeV)	σ (pb)	fac	σ^{excl} (pb)
60	0.0570 (2)	0.45	0.02565 (9)
100	0.0521 (3)	0.5	0.0261 (2)
200	0.0371 (2)	0.8	0.0297 (2)
300	0.0241 (1)	1.02	0.0246 (1)
400	0.00868 (4)	4	0.0347 (2)

Following the same logic as before, we can see that we can naively exclude points where

$$t\bar{t} + E_{\perp} : \sigma \leq 0.0248 \text{ pb}$$

For the search in [28], we use $E_{\perp} \gtrsim 110$ GeV. Cross-sections were calculated as above, and the respective values are given in Table 6.

Table 6. Results for parton-level generation with rudimentary cuts for points which are excluded by $t\bar{t} + E_{\perp}$ searches in [28] via a mediation. Other values are set to $m_H = m_A = m_{H^{\pm}} = 600$ GeV, $m_{\chi} = 1$ GeV, $\cos(\beta - \alpha) = 0$, $\lambda_3 = \lambda_{P_1} = \lambda_{P_2} = 3$, $y_{\chi} = 1$, $\tan \beta = 1$. The factor corresponds to a rough estimate of the multiplicative factor from Figure 15 of that reference. The last column gives the actual exclusion cross-section.

m_a (GeV)	σ (pb)	fac	σ^{excl} (pb)
60	0.2028 (8)	0.24	0.0487 (2)
100	0.1716 (8)	0.25	0.0429 (2)
200	0.1016 (4)	0.5	0.0508 (2)
300	0.0576 (3)	0.8	0.0461 (2)
400	0.01900 (8)	1.4	0.0266 (1)

This leads to

$$t\bar{t} + E_{\perp} : \sigma \leq 0.0268 \text{ pb}$$

for this E_{\perp} cut.

The $b\bar{b}$ final state was investigated in [27] using full Run 2 data. As before, we here use the model file we used in the whole paper, which corresponds to a UV-complete model at a leading order. Again, the mixing angle was set to $\sin \theta = 1/\sqrt{2}$. Values are shown in Table 7. We use $E_{\perp} \geq 180$ GeV, $|p_{\perp,b}| \geq 50$ GeV for the numbers in that table.

Table 7. Results for parton-level generation with rudimentary cuts for points which are excluded by $b\bar{b} + \cancel{E}_\perp$ searches in [27] via a mediation. Other values are set to $m_H = m_A = m_{H^\pm} = 600$ GeV, $m_\chi = 1$ GeV, $\cos(\beta - \alpha) = 0$, $\lambda_3 = \lambda_{P_1} = \lambda_{P_2} = 3$, $y_\chi = 1$, $\tan\beta = 1$. The factor corresponds to a rough estimate of the multiplicative factor from Figure 10 of that reference. The last column gives the actual exclusion cross-section.

m_a (GeV)	σ (pb)	fac	σ^{excl} (pb)
60	0.000860 (4)	20	0.01720 (8)
100	0.000730 (4)	30	0.0219 (1)
200	0.000422 (2)	100	0.0422 (2)
300	0.0002336 (8)	140	0.0327 (1)
500	0.00003536 (8)	400	0.01414 (3)

This leads to

$$b\bar{b} + \cancel{E}_\perp : \sigma \leq 0.01420 \text{ pb}$$

The same channels were investigated in [16] using an integrated luminosity of 36 fb^{-1} . In Tables 8 and 9, we again show the production cross-section for selected points from that reference, as well as the resulting upper bounds on these cross-sections. For $t\bar{t} + \cancel{E}_\perp$, we use $\cancel{E}_\perp \gtrsim 300$ GeV; for $b\bar{b} + \cancel{E}_\perp$, we take $\cancel{E}_\perp \gtrsim 180$ GeV, $p_{\perp,b} \gtrsim 20$ GeV. As in the comparison with the results from [26], we used a slightly different way to generate the event samples for consistency reasons.

Table 8. Results for parton-level generation with rudimentary cuts for points which are excluded by $t\bar{t} + \cancel{E}_\perp$ searches in [16]. Other values are set to $m_H = m_A = m_{H^\pm} = 600$ GeV, $\cos(\beta - \alpha) = 0$, $\lambda_3 = \lambda_{P_1} = \lambda_{P_2} = 3$, $y_\chi = 1$, $\tan\beta = 1$. The factor was taken from HEPData [84]. The last column gives the actual exclusion cross-section.

m_a	m_χ	σ (pb)	fac	σ^{excl} (pb)
70 GeV	1 GeV	0.02536 (8)	1.37	0.0347 (1)
100 GeV	1 GeV	0.02392 (1)	1.41	0.03373 (1)
200 GeV	1 GeV	0.01848 (8)	1.94	0.0359 (2)
300 GeV	1 GeV	0.01292 (8)	2.7	0.0349 (2)
500 GeV	1 GeV	0.00270 (2)	13.65	0.0369 (3)
10 GeV	30 GeV	0.000520 (4) (1)	44.56	0.0232 (2)
10 GeV	50 GeV	0.000368 (4)	63.25	0.0233 (3)
10 GeV	100 GeV	0.000170 (3)	166.52	0.023 (3)
10 GeV	200 GeV	0.000031(4)	736.94	0.0245 (3)
10 GeV	300 GeV	$2.92 (4) \times 10^{-7}$	2346.43	0.000685 (9)
10 GeV	500 GeV	$4.94 (4) \times 10^{-8}$	14 628.82	0.000723 (5)

Table 9. Results for parton-level generation with rudimentary cuts for points which are excluded by $b\bar{b} + \cancel{E}_\perp$ searches in [16]. Other values are set to $m_H = m_{H^\pm} = m_A = 600$ GeV, $m_\chi = 1$ GeV, $\cos(\beta - \alpha) = 0$, $\lambda_3 = \lambda_{P_1} = \lambda_{P_2} = 3$, $y_\chi = 1$, $\tan\beta = 1$. The factor was taken from HEPData [84]. The last column gives the actual exclusion cross-section.

m_a	σ (pb)	fac	σ^{excl} (pb)
70	0.001808 (8)	316.33	0.572 (3)
100	0.001584 (8)	400.243	0.634 (3)
200	0.001044 (4)	876.85	0.915 (4)
300	0.000479 (2)	1875.75	0.898 (4)
500	$6.83(4) \times 10^{-5}$	8581.11	0.586 (3)

Following the same logic as before, we now require that:

$$\sigma_{t\bar{t} + \cancel{E}_\perp} \leq 0.000703 \text{ pb}; \sigma_{b\bar{b} + \cancel{E}_\perp} \leq 0.578 \text{ pb}$$

with the cuts as specified above (note that different cuts apply—furthermore, in [27], the results for $m_a < m_{\chi'}$, which led to quite strong constraints in the analysis in [16], were not presented).

- **Bounds from monojet searches**

We also compared the results for monojet searches as presented in [85]. As discussed above, this work used a different model file, which we accommodated by setting $\sin \theta = \frac{1}{\sqrt{2}}$ and rescaling our result accordingly. Bounds on the signal strength were taken from Hepdata [86]. Our results are presented in Table 10. We applied a cut on the missing transverse energy $\cancel{E}_\perp \gtrsim 250$ GeV.

Table 10. Results for parton-level generation with rudimentary cuts for points which are excluded by monojet searches in [85]. Other values are set to $m_H = m_{H^\pm} = m_A = 600$ GeV, $m_\chi = 1$ GeV, $\cos(\beta - \alpha) = 0$, $\lambda_3 = \lambda_{p_1} = \lambda_{p_2} = 3$, $y_\chi = 1$, $\tan \beta = 1$. For $m_a \geq 500$ GeV, the heavy scalar masses were set to 1 TeV. The factor was taken from HEPData [86]. The last column gives the actual exclusion cross-section.

m_a	σ (pb)	fac	σ^{excl} (pb)
80	0.346 (2)	0.78	0.270 (2)
100	0.3352 (4)	0.76	0.2547 (3)
200	0.2812 (4)	0.69	0.1940 (3)
300	0.277 (2)	0.51	0.141 (1)
350	0.342 (1)	0.36	0.123 (4)
400	0.184 (2)	0.56	0.1028 (9)
450	0.1144 (4)	0.87	0.0995 (3)
500	0.0728 (4)	1.2	0.0874 (5)
600	0.0362 (2)	2.4	0.0868 (4)
700	0.01832 (8)	4.1	0.0751 (3)
800	0.00962 (3)	6.6	0.0636 (2)

The table translates into a maximal allowed cross-section of approximately $\sigma_{\text{lim}} = 0.0638$ pb.

3.4. Dark Matter Constraints

The THDMa renders a dark matter candidate and is therefore subject to constraints from astrophysical measurements, such as relic density and direct detection. We made use of MadDM [87–89] for the calculation of relic density. For direct detection, we implemented the analytic expressions presented in [1] (a more detailed analysis, e.g., such as that presented in [9,12,90,91], was beyond the scope of the current work). We compare these values to limits from the Planck collaboration [92] and require that

$$\Omega h^2 \leq 0.1224 \quad (16)$$

which corresponds to a 2σ limit. Direct detection bounds were compared to maximal cross-section values $\sigma_{\text{max}}^{\text{Xenon1T}}(m_\chi)$ using the XENON1T result [93] which we implemented in terms of an approximation function (the numerical values were obtained using the Phenodata database [94]). Note we rescaled bounds from direct detection according to:

$$\sigma_{\text{max}}(m_{\chi,i}, \Omega_i) = \sigma_{\text{max}}^{\text{Xenon1T}}(m_\chi) \frac{0.1224}{\Omega_i}, \quad (17)$$

where $m_{\chi,i}$, Ω_i referred to the dark matter and relic density of the specific parameter point i tested here.

4. Scan Setup and Results

4.1. Scan Setup

The above constraints were implemented using an interplay of private and publicly available codes in several steps. We discuss these in the following. This also means that, as bounds are successively implemented, subsequent constraints are imposed on the subset of parameter points which passed previous constraints.

1. In a first step, we impose perturbativity, positivity, and perturbative unitarity constraints as discussed in Section 3.1. We also set a lower limit on $\tan\beta$ from the fit function for $B \rightarrow X_s\gamma$ derived in [54,56].
2. Points passing these bounds are then passed on to Spheno, which is used for the calculation of limits from electroweak oblique parameters, $B_s \rightarrow \mu^+\mu^-$, ΔM_s , as well as the total widths for all particles. These values are confronted with the experimental constraints discussed in Section 3.2.
3. The remaining parameter points are now passed through HiggsBounds and HiggsSignals, for comparison with null-results from experimental searches as well as Higgs signal strength measurements which are contained in these tools.
4. We then calculate the relic density as well as the direct detection constraints, which are discussed in Section 3.4.
5. Parameter points which passed all remaining constraints are confronted with the collider bounds presented in Section 3.3.

Our initial scan ranges were determined by a number of prescans to determine the regions of parameter space that are highly populated, while still rendering relatively low masses of up to 1 TeV. In particular, we set:

$$\begin{aligned} \sin\theta &\in [-1;0.8]; \quad \cos(\beta - \alpha) \in [-0.08;0.1]; \quad \tan\beta \in [0.52;9], \\ m_H &\in [500;1000]\text{GeV}, \quad m_A \in [600;1000]\text{GeV}, \quad m_{H^\pm} \in [800;1000]\text{GeV}, \\ m_a &\in [0;m_A], \quad m_\chi \in [0,m_a], \\ y_\chi &\in [-\pi;\pi], \quad \lambda_{P_1} \in [0;10], \quad \lambda_{P_2} \in [0;4\pi], \quad \lambda_3 \in [-2;4\pi]. \end{aligned} \quad (18)$$

The values of $m_h = 125\text{GeV}$ and $v = 246\text{GeV}$ were set according to measurements of the Higgs boson mass as well as the precision measurements. Note that the above choices do not imply that values outside the above regions are strictly forbidden (apart from the bounds we explicitly discuss below), but these were found to render a relatively large acceptance rate for the scan discussed above. We further apply the following relations between masses:

$$\begin{aligned} m_A - m_H &\in [-300;400]\text{GeV}, & m_{H^\pm} - m_H &\in [-150;300]\text{GeV}, & m_A - m_{H^\pm} &\in [-200;200]\text{GeV}, \\ m_a &< m_H + 400\text{GeV}, & m_a &< m_{H^\pm} + 200\text{GeV}, & m_\chi &< m_H - 200\text{GeV}, \\ m_\chi &< m_A - 300\text{GeV}, & m_\chi &< m_{H^\pm} - 400\text{GeV} & m_\chi &< m_a/2 + 50\text{GeV}, \end{aligned}$$

which were superimposed on the original scan ranges (we obviously adjusted the ranges such that all $m_i \geq 0\text{GeV}$). Note that, a priori, points outside the above regions were also allowed; these were chosen to optimize the selection process imposed by the cuts.

Note that the fit for $B \rightarrow X_s\gamma$ implies a lower bound on m_{H^\pm} of $\sim 800\text{GeV}$ (we are aware that using these observables in a fit rather than as hard bounds might weaken some of the constraints discussed here, as, e.g., discussed in [95] for a normal THDM—though this is beyond the scope of the current work).

4.2. Scan Results

In the following, we discuss the resulting constraints on the parameter space of the THDMa. Note that not all bounds discussed above lead to a direct limit in a two-dimensional parameter plane. In case the effects can be displayed in such a simple way, we discuss them explicitly.

We generated $\sim 30\,000$ parameter points in the first step of the above scan. The application of bounds in step 2 includes, e.g., constraints from flavor-physics in the $m_{H^\pm}, \tan\beta$ plane. Results from the flavor constraints in the $m_{H^\pm}, \tan\beta$ plane are shown in Figure 1, where similar results were obtained, e.g., in [52,53,96]. Note that the newest result from the LHC experimental combination for $B_s \rightarrow \mu^+\mu^-$ [57] increases the discrepancy between the experimental result and theory prediction, leading to a larger exclusion region. In the mass range considered here, we found that the limit can be approximated by requiring $\tan\beta \geq 2.15302 - 0.000930233 \frac{m_{H^\pm}}{\text{GeV}}$. Furthermore, in [52], the ΔM_s bound is not shown in the figure for flavor constraints. However, similar results were obtained (T.R. gratefully acknowledges the GFitter authors for clarifying this point).

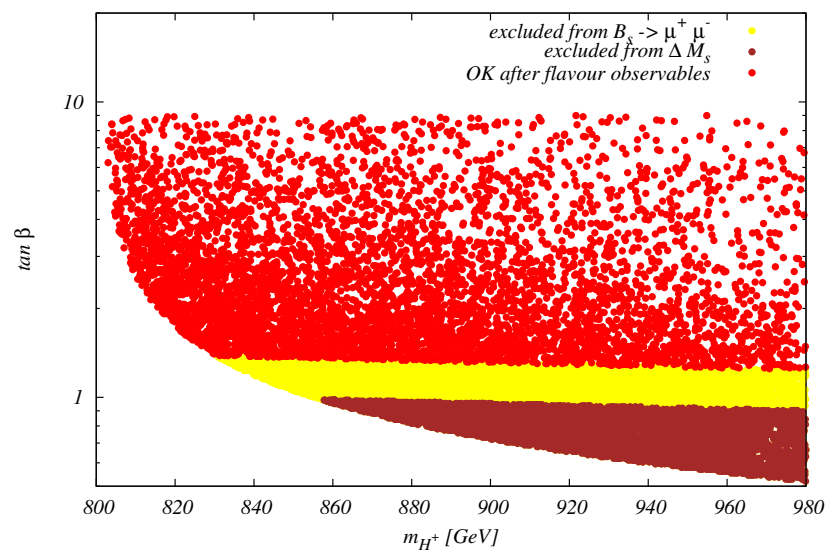


Figure 1. Exclusion in the $(m_{H^\pm}, \tan\beta)$ plane after applying the flavor constraints. The lower bound for $m_{H^\pm} \leq 850$ GeV was set by the bound on $B \rightarrow X_s \gamma$ as discussed in Section 3.2.

After the bounds were imposed by theory, the only constraints we found from widths are points which violate (9). This basically rules out all points with $m_a \leq 62.5$ GeV, as the $h \rightarrow aa$ decay becomes dominant and can lead to large partial widths. Note that the respective coupling does not approach zero for $\sin\theta \rightarrow 0$, but is mediated via λ_{P_1} and λ_{P_2} , cf., e.g., the explicit form of the coupling given in [4]. All other mass ratios are $\Gamma/m \lesssim 28\%$ for all points that fulfill theory constraints, and maximally approximately 24% for Γ_A/m_A after width bounds are included. As an example, the point with the largest allowed ratio features a dominant branching ratio for $A \rightarrow ha$, mediated via relatively large $\tan\beta \sim 8.1$, $\lambda_{P_2} \sim 11.6$ values and masses $m_A = 847$ GeV, $m_a = 298$ GeV. For large values of Γ_H/m_H , typically $H \rightarrow aZ$ and $H \rightarrow t\bar{t}$ are dominant, with $m_H \gtrsim 800$ GeV, $|\sin\theta| \sim 0.35 - 0.65$. Large widths for a typically stem from large $|y_\chi| \sim 1.8$ and small $|\sin\theta| \lesssim 0.2$ values, corresponding to the coupling determining the $a \rightarrow \chi\bar{\chi}$ decay [4]. Electroweak precision observables, on the other hand, have an impact on the allowed mass splittings, such that, for example, regions with $|m_{H^\pm} - m_A| \gtrsim 190$ GeV are basically forbidden. In fact, we see largest deviations in the oblique parameters trace back to excessively large absolute values of the T-parameter, i.e., $T \lesssim -0.03$, where the largest values stem from $|m_{H^\pm} - m_H| \gtrsim 250$ GeV. Such deviations typically stem from new physics contributions to gauge-boson propagators, which are therefore sensitive to mass differences. As an example, we show the exclusion in the $(m_{H^\pm} - m_H, m_{H^\pm} - m_A)$ and $(m_{H^\pm} - m_H, m_H - m_A)$ planes in Figure 2. Another interesting parameter plane is given by $(m_a, |\sin\theta|)$, where the oblique parameters also set a clear limit, as can be seen in Figure 3. We also investigated how our results compare to the ones obtained in the THDM limit, where a is decoupled. This can be achieved by setting $\sin\theta = \lambda_{P_1} = \lambda_{P_2} = 0$. We

then compared the limits in the $(m_{H^\pm} - m_A, m_H - m_A)$ plane, cf. Figure 4. We see that the admixture of a leads to much weaker constraints on $m_{H^\pm} - m_A$. For the remaining constraints discussed in Section 3.2, the identification of additional regions in the two-dimensional parameter planes that are primarily affected is not straightforward.

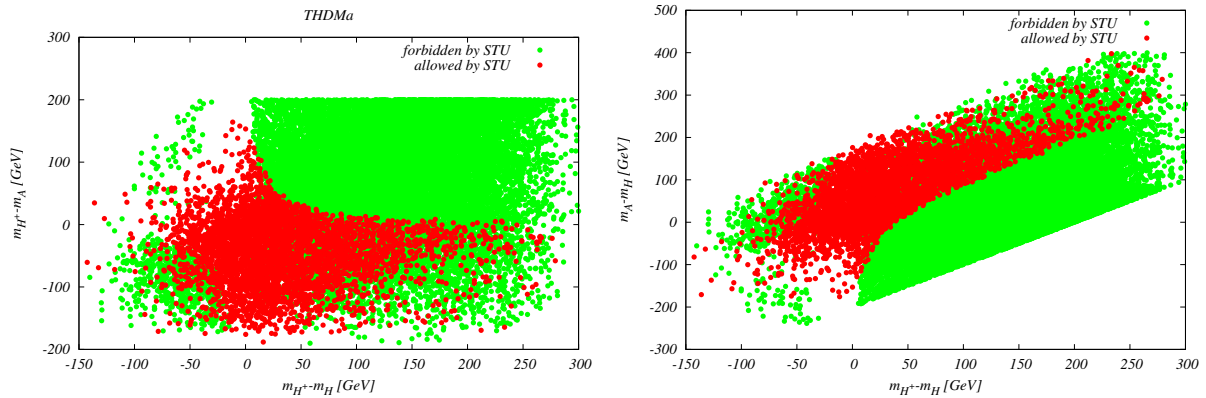


Figure 2. Exclusions in the $(m_{H^\pm} - m_H, m_{H^\pm} - m_A)$ (left) and $(m_{H^\pm} - m_H, m_H - m_A)$ (right) planes from oblique parameters. We see that regions where both displayed mass differences are large are excluded by the oblique parameters.

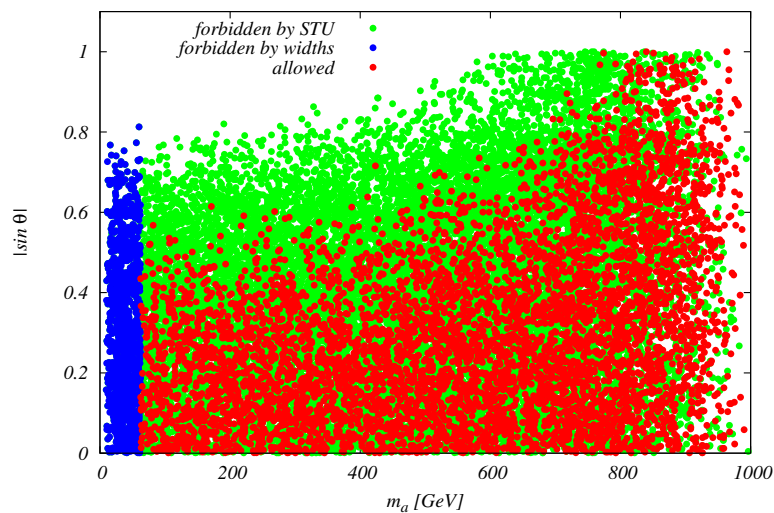


Figure 3. Exclusion in the $(m_a, |\sin \theta|)$ plane from oblique parameters. Limits from setting an upper bound on the total width of the 125 GeV scalar (Equation (9)) are also shown.

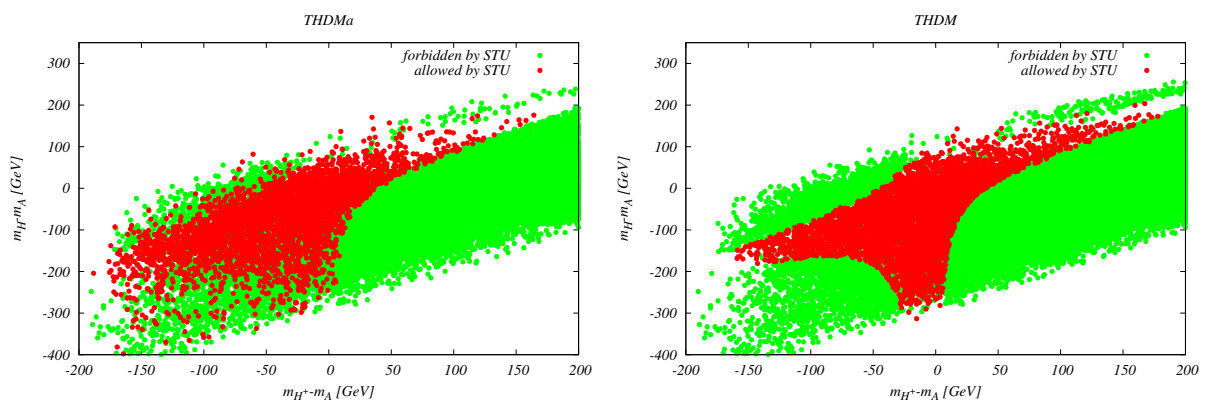


Figure 4. Exclusions in the $(m_{H^\pm} - m_A, m_H - m_A)$ plane in the THDMa (left) and THDM (right) from oblique parameters; for the latter, $\sin \theta = \lambda_{P_1} = \lambda_{P_2} = 0$. The admixture of a releases the bounds, as expected.

We now turn to the effects of applying collider constraints via HiggsBounds/HiggsSignals. As expected in THDMs and its extensions, only narrow stripes around $\cos(\beta - \alpha) = 0$ remain in agreement with current signal strength measurements (as can be seen, e.g., [97, 98]).

Using the tools described above, we find the allowed/forbidden areas in the $(\cos(\beta - \alpha), \tan \beta)$ plane as shown in Figure 5. Comparing this to the results presented, e.g., in [99,100], we see that the constraints for negative values of $\cos(\beta - \alpha)$ agree, while we find more stringent constraints for positive values. However, note that we use different approaches, and for example, HiggsSignals makes use of the most recent constraints as well as STXS information [101]. We thank the authors of [99] for useful correspondence concerning this point. Some points are additionally ruled out by $H/a \rightarrow \tau\tau$ [102], $H \rightarrow h_{125}h_{125}$ [103] and $H \rightarrow aZ$ [104,105] searches. Values of $\cos(\beta - \alpha) > 0.04$ and $\tan \beta \gtrsim 5$ are excluded from $h_{125} \rightarrow ZZ$ [106]. Points which are still allowed after the application of HiggsBounds and HiggsSignals are outside the region sensitive to the full Run 2 $A \rightarrow HZ$ search [107], assuming on-shell production and decay. We tested this by comparing this to cross-sections for $pp \rightarrow A \rightarrow ZH$ production and successive decays $H \rightarrow b\bar{b}$ from Figure 10 in that reference.. Furthermore, the region where $\cos(\beta - \alpha) \lesssim -0.05$, $\tan \beta \gtrsim 5$ is mainly ruled out from both perturbative unitarity and perturbativity.

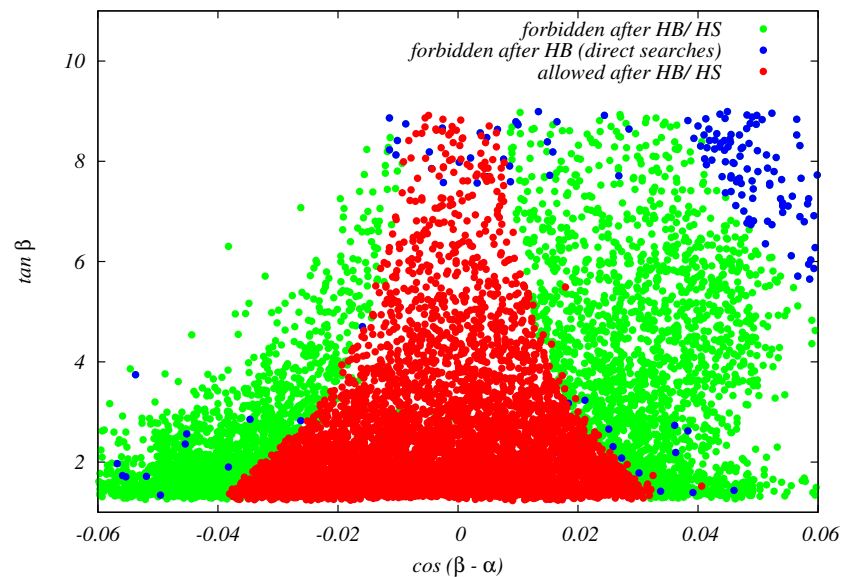


Figure 5. Exclusion in the $\cos(\beta - \alpha), \tan \beta$ plane after HiggsBounds (HB) and HiggsSignals (HS).

Constraints from relic density, i.e., the requirement that Equation (16) is fulfilled, depends on many parameters. In general, however, small values of $|m_a - 2m_\chi|$ can trigger efficient annihilation processes via the resonant s-channel diagram, and lead to relic density values between 10^{-6} and the upper bound. For larger mass differences $\mathcal{O}(200\text{ GeV})$ or larger, basically all points are excluded. Dominant annihilation channels are $\chi\bar{\chi} \rightarrow b\bar{b}$ and $\chi\bar{\chi} \rightarrow t\bar{t}$, where the latter channel opens up for $m_a \gtrsim 2m_t$ and tends to lead to smaller values of relic density. We show the values of relic density as a function of the above mass difference in Figure 6.

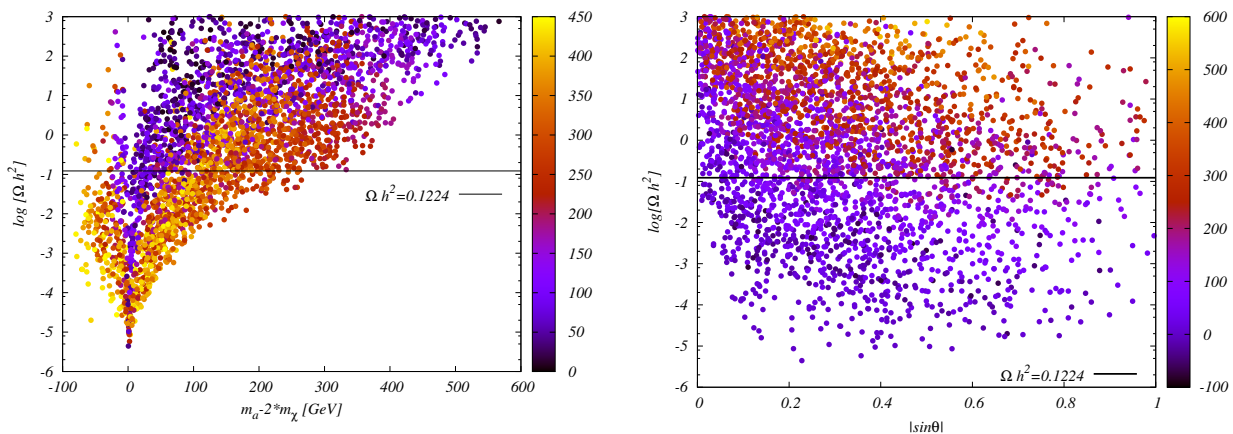


Figure 6. (Left): Relic density as a function of $m_a - 2m_\chi$ with the color coding referring to the mass of the DM candidate. Heavier m_χ tends to lead to smaller values of the relic density. (Right): Relic density as a function of $|\sin\theta|$, with the color coding referring to the mass difference $m_a - 2m_\chi$. Lower values of $|\sin\theta|$ lead to smaller annihilation cross-sections and therefore larger values of relic density.

Similarly, for $\sin\theta \rightarrow 0$ annihilation cross-sections tend to become small, such that relic density predictions exceed the value measured by the Planck collaboration, cf. Equation (16). We display the dependence on this variable in Figure 6, where in addition, color coding indicates the mass difference $m_a - 2m_\chi$.

Considering only points that pass the relic density constraints, we found that direct detection does not impose any additional constraints. A more detailed analysis, as, e.g., presented in [9,12,90,91], could modify this statement. However, from Figure 24 in [6], we see that these constraints are only effective for masses $m_a \lesssim 60$ GeV and additionally depend on the mixing angle. We verified that the few points that feature this in mass range are not excluded when compared to the above figure. Further comments on the sensitivity of future direct detection experiments for this model can, e.g., be found in [12].

Before discussing the constraints from direct searches, we will briefly summarize the effects that the bounds considered above have imposed on the original parameter space:

- B-physics constraints set a lower bound on $\tan\beta$ as a function of m_{H^\pm} ; in general, $\tan\beta > 1$;
- Signal strength measurements reduced the available parameter space for $\cos(\beta - \alpha)$, such that now $\cos(\beta - \alpha) \in [-0.04; 0.04]$;
- Relic density reduced the available parameter space to regions where $m_a - 2m_\chi \in [-100; 300]$ GeV;
- Furthermore, oblique parameters reduce the allowed mass differences, especially in the THDM scalar sector;
- In the general scan, the upper limits of m_a in dependence on m_H, m_{H^\pm} are also reduced by more than 100 GeV. However, this is an artifact of the scan, and one can easily repopulate these regions in a more fine-tuned setup;
- We also see that $m_H > 550$ GeV, $m_A > 750$ GeV. In both cases, a large number of points are excluded from S, T, U observables, as these variables favor small mass differences between the new scalars. If we force $m_A \leq 750$ GeV, for example, out of 1000 points, only one survives which has very degenerate m_H, m_{H^\pm} masses, differing on the permill level. If we force $m_H \leq 550$ GeV, more points survive, which feature a small m_{H^\pm}, m_A difference, typically $\lesssim 10\%$ difference, as well as small mass differences $|m_a - 2m_\chi| \lesssim 120$ GeV. In a general, non-fine-tuned scan, the lower bound on m_{H^\pm} forces the mass scale of H, A to be $\gtrsim 530 - 550$ GeV.

All other parameters still populate the original regions set in Equation (18).

Regarding direct collider constraints as discussed in Section 3.3, we find the following results

- The strongest constraints stem from $h + \cancel{E}_\perp$ searches presented in [32], cutting out approximately $\sim 28\%$ of the leftover parameter space. As we let all parameters float freely, limits on the 2-dimensional planes are not straightforward. Using our approach, only points for which $m_a - 2m_\chi \geq 0$ are affected. Furthermore, points where $m_\chi \geq 400$ GeV are not affected. This, however, is, e.g., due to a strong correlation between m_χ and m_a , which in turn influences the mass difference $m_A - m_a$ and the $A \rightarrow ha$ branching ratio;
- The $\ell\ell + \cancel{E}_\perp$ searches cut out roughly 9% of the available parameter space. As in [22], regions with $m_a \lesssim 500$ GeV are mainly affected. However, as we scan over all parameters, also many points for which $m_a \lesssim 500$ GeV are still allowed. In addition, the branching ratio for $H \rightarrow aZ$ swiftly goes to 0 when $m_H - m_a \rightarrow m_Z$, and only has reasonably large values when $m_H - m_a \gtrsim 200$ GeV so that only points obeying this mass hierarchy are excluded. Similarly, as the above branching ratio $\sim \sin^2 \theta$, we found that points for which $|\sin \theta| \lesssim 0.15$ are not excluded.
- The bounds from the $pp \rightarrow H^+ \bar{t}b, H^+ \rightarrow \bar{t}t$ searches [25] do not constrain the parameter space here, as production cross-sections for the process $pp \rightarrow H^+ \bar{t}b$ are $\mathcal{O}(10^{-2}$ pb). This can be traced back to the lower limit on $\tan \beta$ from B-physics observables, cf. Figure 1. The same holds for searches in the same production mode, but with different final states [30].
- Searches for $t\bar{t} + \cancel{E}_\perp$ cut out a relatively small region of parameter space, $\sim 1\%$, in the range where $m_a \lesssim 300$ GeV, $m_a - 2m_\chi \in [0; 40]$ GeV, $\tan \beta \lesssim 2$. As before, several parameters contribute, so one also finds allowed points within the regions mentioned above. All of these are also subject to at least one other constraint from the searches mentioned above.
- None of the points were excluded by the $W^+ \bar{t} + \cancel{E}_\perp / W^- t + \cancel{E}_\perp, b\bar{b} + \cancel{E}_\perp$ and the monojet searches considered here.

5. Predictions for e^+e^- Colliders

Out of the remaining parameter space, we now investigate the magnitude of expected rates at possible future e^+e^- colliders. In the limit where $\sin \theta \rightarrow 0$, we recover the decoupling scenario of a standard THDM. It is therefore interesting whether we can find regions in parameter space where novel signatures, and explicitly final states with missing energy, give the largest rates.

If we focus on the neutral sector and pair-production processes, possible final states are given by ha, hA, HA, Ha . For the first two processes, the sum of masses remains $\lesssim 1$ TeV, so colliders with a center-of-mass energy in that range might be relevant. For the latter two, on the other hand, masses can range above 1 TeV, and we can consider cross-sections at a 3 TeV collider.

Note that $h[H]A$ production in a THDM is mainly mediated via Z-boson exchange in the s-channel, where the corresponding coupling is proportional to $\cos(\beta - \alpha) [\sin(\beta - \alpha)]$, respectively. As $\cos(\beta - \alpha)$ is heavily constrained, the corresponding cross-sections are quite small, reaching $\mathcal{O}(10^{-3}$ fb). Therefore, we will here concentrate on $HA(a)$ production and decay. For this channel, we find that at a 3 TeV collider, production cross-sections can reach up to 1 fb, where largest cross-section values are achieved for $m_A + m_H \sim 1400$ GeV. Dominant decay modes for such points are displayed in Figure 7.

Decays without missing energy lead to $t\bar{t}\bar{t}$ and $t\bar{t}t\bar{t}Z$ final states, where the first is dominant in large regions of parameter space. The first decay mode that is novel with respect to standard THDMs is the $t\bar{t} + \cancel{E}$ final state. In order to identify regions where this state dominates, we show the expected $t\bar{t}\bar{t}$ and $t\bar{t} + \cancel{E}$ cross-sections in Figure 8, where in the right plot, we additionally include contributions mediated via Ha production.

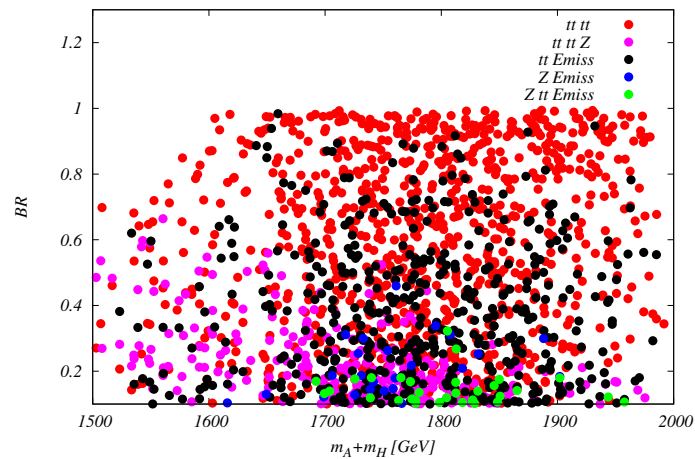


Figure 7. Combined branching ratios for HA final states as a function of the mass sum.

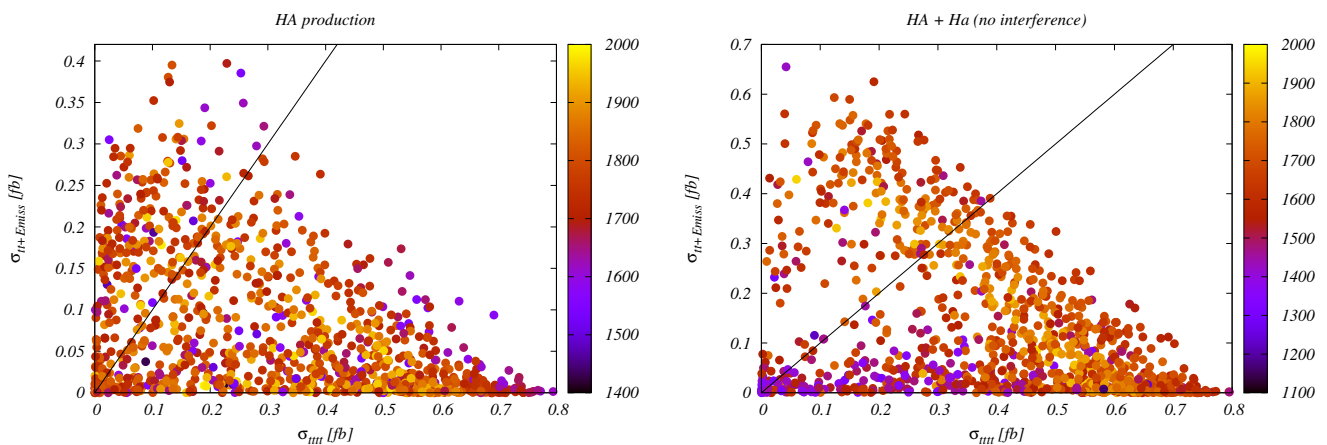


Figure 8. Production cross-sections for $t\bar{t}t\bar{t}$ and $t\bar{t} + \cancel{E}$ final states, using a factorized approach. (Left:) via HA and (right:) via $HA + Ha$ production. Color coding refers to the mass scale, which is defined as $m_H + m_A$ (left)/ $m_H + 0.5 \times (m_A + m_a)$ (right), respectively.

We see that we can indeed identify regions where $t\bar{t} + \cancel{E}$ dominates and renders the largest rates. As an example, we here list the parameters of the “best point”:

$$\begin{aligned} \sin \theta &= -0.626, \quad \cos(\beta - \alpha) = 0.0027, \quad \tan \beta = 3.55 \\ m_H &= 643 \text{ GeV}, \quad m_A = 907 \text{ GeV}, \quad m_{H^\pm} = 814 \text{ GeV}, \\ m_a &= 653 \text{ GeV}, \quad m_\chi = 277 \text{ GeV}, \\ y_\chi &= -1.73, \quad \lambda_{P_1} = 0.18, \quad \lambda_{P_2} = 2.98, \quad \lambda_3 = 8.63. \end{aligned} \quad (19)$$

The total widths are given by $\Gamma_H = 2.41 \text{ GeV}$, $\Gamma_A = 52.5 \text{ GeV}$, $\Gamma_a = 26.5 \text{ GeV}$, $\Gamma_{H^\pm} = 12.1 \text{ GeV}$, rendering all width/mass ratios $\lesssim 6\%$. The production cross-sections at 3 TeV are given by $\sigma_{HA} = 0.512 \text{ fb}$, $\sigma_{Ha} = 0.390 \text{ fb}$. The H decays to $t\bar{t}$ with a branching ratio of 93%, while $\chi\bar{\chi}$ final states have branching ratios of 64%/95% for A/a , respectively. This leads to an overall estimated production cross-section of approximately 0.65 fb, using factorization and neglecting the possible interference effects. The next step in this investigation would be a detailed simulation of signal and background in a CLIC-like environment, as, e.g., performed in [108,109] for the inert doublet model. This is in the line of future work.

6. Summary and Outlook

In this work, we for the first time presented a scan for the THDMa that lets all 12 free parameters of that model float freely within ranges that were chosen to optimize scan performance. We identified regions in parameter space that survived all current theoretical and experimental constraints, and provided a first estimate of possible production cross-sections within this model at future e^+e^- facilities, with a focus on signatures not present in a standard THDM. We included direct LHC search results using a simplified approach, with maximal cross-sections as an upper limit. Such searches typically constrain the low-mass regions of parameter space, where the dark sector masses are $\lesssim 500$ GeV, as well as regions with mixings $|\sin\theta| \gtrsim 0.15$. In general, however, clear boundaries in two-dimensional planes are not easy to identify. An exception are constraints from B-physics observables, that especially impose a lower limit on the charged mass ~ 800 GeV that varies with $\tan\beta$. Furthermore, constraints from electroweak precision observables in the form of oblique parameters pose relatively strong constraints on the mass differences in the THDMa scalar sector for novel scalars, leading to a general lower mass scale ~ 500 GeV. Requiring the relic density to lie below the current experimental measurement further poses strong constraints on $|m_a - 2m_\chi|$.

We consider this work to be a first step towards a more detailed analysis of this model. This includes more detailed recasts of the current LHC experimental results, including possible forecasts for HL-LHC sensitivity, as well as more detailed investigations at future lepton machines, as, e.g., CLIC or possible muon-colliders. First estimates for the former show that the most promising novel channel could be $t\bar{t} + \cancel{E}$ in a CLIC-like scenario with a 3 TeV center-of-mass energy.

Finally, in view of recent events [110], one might wonder whether the anomalous magnetic momentum of the muon can be explained by the model discussed here. Contributions should be similar to the ones of a general THDM of type II, as, e.g., discussed in [111,112], with additional contributions of the second pseudoscalar a , including appropriate rescaling. However, from the above work, it becomes obvious that pseudoscalar masses would have to be light, $\lesssim 200$ GeV, with additionally relatively large $\tan\beta$ values $\gtrsim 15$, in order to account for the observed experimental value. Such points were not included in our analysis here. A quick check using the next-to-leading order approximation given in [113] shows that maximal values of $\Delta a_\mu^{\text{BSM}} \sim 2.5 \times 10^{-12}$ can be achieved with, e.g., the points which pass all other (including experimental LHC) constraints, which is approximately three orders of magnitude lower than the observed discrepancy. In [52], regions are shown in the $(m_{H^\pm}, \tan\beta)$ plane; here, for charged masses $\gtrsim 800$ GeV, $\tan\beta \gtrsim 7$ seems to be required for 68% confidence level agreement with the result from [114]. This could a priori be an interesting region to investigate, which we will leave for future work.

Funding: This research was supported in parts by the National Science Centre, Poland, the HARMONIA project under contract UMO-2015/18/M/ST2/00518 (2016–2021), and the OPUS project under contract UMO-2017/25/B/ST2/00496 (2018–2021).

Institutional Review Board Statement: Not applicable.

Informed Consent Statement: Not applicable.

Data Availability Statement: Data available upon request.

Acknowledgments: The author wants to sincerely thank J. Kalinowski, W. Kotlarski, D. Sokolowska, and A.F. Zarnecki for useful discussions at the beginning of this project, and especially W. Kotlarski for help with the setup of the Sarah/Spheno interface. Further thanks go to M. Misiak and U. Nierste for discussions regarding bounds from B-physics observables, and M. Goodsell as well as the authors of [12] for advice.

Conflicts of Interest: The author declares no conflict of interest.

Appendix A. Potential Parameters

The potential parameters can be expressed in terms of the free input parameters as follows:

$$\mu_3 = \frac{1}{2}s_{2\alpha}(m_h^2 - m_H^2) - m_{H^\pm}^2 s_{2\beta} + \frac{v^2}{2}\lambda_3 s_{2\beta} \quad (\text{A1})$$

$$\lambda_1 = \frac{s_\alpha s_{\alpha+\beta}}{2v^2 c_\beta^3} m_h^2 + \frac{c_\alpha c_{\alpha+\beta}}{2v^2 c_\beta^3} m_H^2 - \frac{t_\beta^2}{v^2} m_{H^\pm}^2 + \frac{t_\beta^2}{2}\lambda_3 \quad (\text{A2})$$

$$\lambda_2 = \frac{c_\alpha s_{\alpha+\beta}}{2v^2 s_\beta^3} m_h^2 - \frac{s_\alpha c_{\alpha+\beta}}{2v^2 s_\beta^3} m_H^2 - \frac{1}{v^2 t_\beta^2} m_{H^\pm}^2 + \frac{1}{2t_\beta^2}\lambda_3 \quad (\text{A3})$$

$$\lambda_5 = -\frac{1}{2v^2} \left(-2m_{H^\pm}^2 + v^2\lambda_3 + m_A^2 c_\theta^2 + m_a^2 s_\theta^2 + (m_h^2 - m_H^2) \frac{s_{2\alpha}}{s_{2\beta}} \right) \quad (\text{A4})$$

$$\lambda_4 = \frac{1}{v^2} \left(m_A^2 c_\theta^2 + m_a^2 s_\theta^2 - v^2\lambda_3 + (m_H^2 - m_h^2) \frac{s_{2\alpha}}{s_{2\beta}} \right) \quad (\text{A5})$$

$$b_p = \frac{(m_a^2 - m_A^2)c_\theta s_\theta}{v} \quad (\text{A6})$$

$$m_P^2 = m_a^2 c_\theta^2 + m_A^2 s_\theta^2 - v^2(\lambda_{p1} c_\beta^2 + \lambda_{p2} s_\beta^2) \quad (\text{A7})$$

References

- Ipek, S.; McKeen, D.; Nelson, A.E. A Renormalizable Model for the Galactic Center Gamma Ray Excess from Dark Matter Annihilation. *Phys. Rev.* **2014**, *D90*, 055021, doi:10.1103/PhysRevD.90.055021.
- No, J.M. Looking through the pseudoscalar portal into dark matter: Novel mono-Higgs and mono-Z signatures at the LHC. *Phys. Rev.* **2016**, *D93*, 031701, doi:10.1103/PhysRevD.93.031701.
- Goncalves, D.; Machado, P.A.N.; No, J.M. Simplified Models for Dark Matter Face their Consistent Completions. *Phys. Rev.* **2017**, *D95*, 055027, doi:10.1103/PhysRevD.95.055027.
- Bauer, M.; Haisch, U.; Kahlhoefer, F. Simplified dark matter models with two Higgs doublets: I. Pseudoscalar mediators. *J. High Energy Phys.* **2017**, *5*, 138, doi:10.1007/JHEP05(2017)138.
- Tunney, P.; No, J.M.; Fairbairn, M. Probing the pseudoscalar portal to dark matter via $\bar{b}bZ(\rightarrow \ell\ell) + \cancel{E}_T$: From the LHC to the Galactic Center excess. *Phys. Rev.* **2017**, *D96*, 095020, doi:10.1103/PhysRevD.96.095020.
- Abe, T.; Afik, Y.; Albert, A.; Anelli, C.R.; Barak, L.; Bauer, M.; Behr, J.K.; Bell, N. F.; Boveia, A.; Brandt, O.; et al. LHC Dark Matter Working Group: Next-generation spin-0 dark matter models. *Phys. Dark Univ.* **2020**, *27*, 100351, doi:10.1016/j.dark.2019.100351.
- Pani, P.; Polesello, G. Dark matter production in association with a single top-quark at the LHC in a two-Higgs-doublet model with a pseudoscalar mediator. *Phys. Dark Univ.* **2018**, *21*, 8–15, doi:10.1016/j.dark.2018.04.006.
- Haisch, U.; Kamenik, J.F.; Malinauskas, A.; Spira, M. Collider constraints on light pseudoscalars. *J. High Energy Phys.* **2018**, *3*, 178, doi:10.1007/JHEP03(2018)178.
- Abe, T.; Fujiwara, M.; Hisano, J. Loop corrections to dark matter direct detection in a pseudoscalar mediator dark matter model. *J. High Energy Phys.* **2019**, *2*, 028, doi:10.1007/JHEP02(2019)028.
- Haisch, U.; Polesello, G. Searching for dark matter in final states with two jets and missing transverse energy. *J. High Energy Phys.* **2019**, *2*, 128, doi:10.1007/JHEP02(2019)128.
- Haisch, U.; Polesello, G. Searching for production of dark matter in association with top quarks at the LHC. *J. High Energy Phys.* **2019**, *2*, 029, doi:10.1007/JHEP02(2019)029.
- Abe, T.; Fujiwara, M.; Hisano, J.; Shoji, Y. Maximum value of the spin-independent cross section in the 2HDM+a. *J. High Energy Phys.* **2020**, *1*, 114, doi:10.1007/JHEP01(2020)114.
- Butterworth, J.M.; Habedank, M.; Pani, P.; Vaitkus, A. A study of collider signatures for two Higgs doublet models with a Pseudoscalar mediator to Dark Matter. *SciPost Phys. Core* **2021**, *4*, 003, doi:10.21468/SciPostPhysCore.4.1.003.
- Arcadi, G.; Busoni, G.; Hügler, T.; Tenorth, V.T. Comparing 2HDM + Scalar and Pseudoscalar Simplified Models at LHC. *J. High Energy Phys.* **2020**, *6*, 098, doi:10.1007/JHEP06(2020)098.
- Argyropoulos, S.; Brandt, O.; Haisch, U. Collider Searches for Dark Matter through the Higgs Lens. *arXiv* **2021**, arXiv:2109.13597.
- Aaboud, M.; Aad, G.; Abbott, B.; Abdinov, O.; Abeloos, B.; Abidi, S.H.; AbouZeid, O.S.; Abraham, N.L.; Abramowicz, H.; Abreu, H.; et al. Search for dark matter produced in association with bottom or top quarks in $\sqrt{s} = 13$ TeV pp collisions with the ATLAS detector. *Eur. Phys. J.* **2018**, *C78*, 18, doi:10.1140/epjc/s10052-017-5486-1.

17. Sirunyan, A.M.; Tumasyan, A.; Adam, W.; Ambrogio, F.; Asilar, E.; Bergauer, T.; Brandstetter, J.; Dragicevic, M.; Erö, J.; Del Valle, A.E.; et al. Search for dark matter produced in association with a Higgs boson decaying to a pair of bottom quarks in proton–proton collisions at $\sqrt{s} = 13$ TeV. *Eur. Phys. J. C* **2019**, *79*, 280, doi:10.1140/epjc/s10052-019-6730-7.
18. Aaboud, M.; Aad, G.; Abbott, B.; Abdinov, O.; Abeloos, B.; Abhayasinghe, D.K.; Abidi, S.H.; AbouZeid, O.S.; Abraham, N.L.; Abramowicz, H.; et al.; Search for Higgs boson decays into a pair of light bosons in the $b\bar{b}\mu\mu$ final state in pp collision at $\sqrt{s} = 13$ TeV with the ATLAS detector. *Phys. Lett.* **2019**, *B790*, 1–21, doi:10.1016/j.physletb.2018.10.073.
19. Aaboud, M.; Aad, G.; Abbott, B.; Abdinov, O.; Abeloos, B.; Abidi, S.H.; AbouZeid, O.S.; Abraham, N.L.; Abramowicz, H.; Abreu, H.; et al. Search for Higgs boson decays to beyond-the-Standard-Model light bosons in four-lepton events with the ATLAS detector at $\sqrt{s} = 13$ TeV. *J. High Energy Phys.* **2018**, *6*, 166, doi:10.1007/JHEP06(2018)166.
20. Aaboud, M.; Aad, G.; Abbott, B.; Abdinov, O.; Abeloos, B.; Abhayasinghe, D.K.; Abidi, S.H.; AbouZeid, O.S.; Abraham, N.L.; Abramowicz, H.; et al. Constraints on mediator-based dark matter and scalar dark energy models using $\sqrt{s} = 13$ TeV pp collision data collected by the ATLAS detector. *J. High Energy Phys.* **2019**, *5*, 142, doi:10.1007/JHEP05(2019)142.
21. Sirunyan, A.M.; Tumasyan, A.; Adam, W.; Ambrogio, F.; Bergauer, T.; Brandstetter, J.; Dragicevic, M.; Erö, J.; Valle, A.E.D.; Flechl, M.; et al. Search for dark matter particles produced in association with a Higgs boson in proton-proton collisions at $\sqrt{s} = 13$ TeV. *JHEP* **2020**, *3*, 025, doi:10.1007/JHEP03(2020)025.
22. Sirunyan, A.M.; Tumasyan, A.; Adam, W.; Bergauer, T.; Dragicevic, M.; Eroo, J.; Escalante Del Valle, A.; Fruehwirth, R.; Jeitler, M.; Krammer, N.; et al.; Search for dark matter produced in association with a leptonically decaying Z boson in proton-proton collisions at $\sqrt{s} = 13$ TeV. *Eur. Phys. J.* **2021**, *C81*, 13, doi:10.1140/epjc/s10052-020-08739-5.
23. Aad, G.; Abbott, B.; Abbott, D.C.; Abed Abud, A.; Abeling, K.; Abhayasinghe, D.K.; Abidi, S.H.; AbouZeid, O.S.; Abraham, N.L. Search for dark matter produced in association with a single top quark in $\sqrt{s} = 13$ TeV pp collisions with the ATLAS detector. *Eur. Phys. J. C* **2021**, *81*, 860, doi:10.1140/epjc/s10052-021-09566-y.
24. Aad, G.; Abbott, B.; Abbott, D.C.; Abed Abud, A.; Abeling, K.; Abhayasinghe, D.K.; Abidi, S.H.; AbouZeid, O.S.; Abraham, N.L.; Abramowicz, H.; et al. Search for Higgs boson decays into two new low-mass spin-0 particles in the $4b$ channel with the ATLAS detector using pp collisions at $\sqrt{s} = 13$ TeV. *Phys. Rev.* **2020**, *D102*, 112006, doi:10.1103/PhysRevD.102.112006.
25. Aad, G.; Abbott, B.; Abbott, D.C.; Abed Abud, A.; Abeling, K.; Abhayasinghe, D.K.; Abidi, S.H.; AbouZeid, O.S.; Abraham, N.L.; Abramowicz, H.; et al. Search for dijet resonances in events with an isolated charged lepton using $\sqrt{s} = 13$ TeV proton-proton collision data collected by the ATLAS detector. *J. High Energy Phys.* **2020**, *6*, 151, doi:10.1007/JHEP06(2020)151.
26. Aad, G.; Abbott, B.; Abbott, D.C.; Abed Abud, A.; Abeling, K.; Abhayasinghe, D.K.; Abidi, S.H.; AbouZeid, O.S.; Abraham, N.L.; Abramowicz, H.; et al. Search for new phenomena with top quark pairs in final states with one lepton, jets, and missing transverse momentum in pp collisions at $\sqrt{s} = 13$ TeV with the ATLAS detector. *J. High Energy Phys.* **2021**, *4*, 174, doi:10.1007/JHEP04(2021)174.
27. Aad, G.; Abbott, B.; Abbott, D.C.; Abed Abud, A.; Abeling, K.; Abhayasinghe, D.K.; Abidi, S.H.; AbouZeid, O.S.; Abraham, N.L.; Abramowicz, H.; et al. Search for new phenomena in final states with b -jets and missing transverse momentum in $\sqrt{s} = 13$ TeV pp collisions with the ATLAS detector. *J. High Energy Phys.* **2021**, *5*, 093, doi:10.1007/JHEP05(2021)093.
28. Aad, G.; Abbott, B.; Abbott, D.C.; Abed Abud, A.; Abeling, K.; Abhayasinghe, D.K.; Abidi, S.H.; AbouZeid, O.S.; Abraham, N.L.; Abramowicz, H.; et al. Search for new phenomena in events with two opposite-charge leptons, jets and missing transverse momentum in pp collisions at $\sqrt{s} = 13$ TeV with the ATLAS detector. *J. High Energy Phys.* **2021**, *4*, 165, doi:10.1007/JHEP04(2021)165.
29. Aad, G.; Abbott, B.; Abbott, D.C.; Abed Abud, A.; Abeling, K.; Abhayasinghe, D.K.; Abidi, S.H.; Aboulhorma, A.; Abramowicz, H.; Abreu, H.; et al. Search for Higgs boson decays into a pair of pseudoscalar particles in the $b\bar{b}\mu\mu$ final state with the ATLAS detector in pp collisions at $\sqrt{s} = 13$ TeV. *arXiv* **2021**, arXiv:2110.00313.
30. Aad, G.; Abbott, B.; Abbott, D.C.; Abed Abud, A.; Abeling, K.; Abhayasinghe, D.K.; Abidi, S.H.; AbouZeid, O.S.; Abraham, N.L.; Abramowicz, H.; et al. Search for charged Higgs bosons decaying into a top quark and a bottom quark at $\sqrt{s} = 13$ TeV with the ATLAS detector. *J. High Energy Phys.* **2021**, *6*, 145, doi:10.1007/JHEP06(2021)145.
31. Aad, G.; Abbott, B.; Abbott, D.C.; Abed Abud, A.; Abeling, K.; Abhayasinghe, D.K.; Abidi, S.H.; AbouZeid, O.S.; Abraham, N.L.; Abramowicz, H.; et al. Search for dark matter in events with missing transverse momentum and a Higgs boson decaying into two photons in pp collisions at $\sqrt{s} = 13$ TeV with the ATLAS detector. *J. High Energy Phys.* **2021**, *10*, 013, doi:10.1007/JHEP10(2021)013.
32. Aad, G.; Abbott, B.; Abbott, D.C.; Abed Abud, A.; Abeling, K.; Abhayasinghe, D.K.; Abidi, S.H.; Aboulhorma, A.; Abramowicz, H.; Abreu, H.; et al. Search for dark matter produced in association with a Standard Model Higgs boson decaying into b -quarks using the full Run 2 dataset from the ATLAS detector. *arXiv* **2021**, arXiv:2108.13391.
33. Aad, G.; Abbott, B.; Abbott, D.C.; Abed Abud, A.; Abeling, K.; Abhayasinghe, D.K.; Abidi, S.H.; Aboulhorma, A.; Abramowicz, H.; Abreu, H.; et al. Search for associated production of a Z boson with an invisibly decaying Higgs boson or dark matter candidates at $\sqrt{s} = 13$ TeV with the ATLAS detector. *arXiv* **2021**, arXiv:2111.08372.
34. The ATLAS Collaboration. *Combination and Summary of ATLAS Dark Matter Searches Using 139 fb⁻¹ of $\sqrt{s} = 13$ TeV pp Collision Data and Interpreted in a Two-Higgs-Doublet Model with a Pseudoscalar Mediator*; Technical Report; All Figures Including Auxiliary Figures; CERN: Geneva, Switzerland, 2021; Available online: <https://atlas.web.cern.ch/Atlas/GROUPS/PHYSICS/CONFNOTES/ATLAS-CONF-2021-036> (accessed on 6 August 2021).
35. The CMS Collaboration. *Projection of the Mono-Z Search for Dark Matter to the HL-LHC*; Technical Report CMS-PAS-FTR-18-007; CERN: Geneva, Switzerland, 2018.

36. ATLAS sensitivity to Two-Higgs-Doublet models with an additional pseudoscalar exploiting four top quark signatures with $3ab^{-1}$ of $\sqrt{s} = 14$ TeV proton-proton collisions. Technical Report; All Figures Including Auxiliary Figures; CERN, Geneva, 2018; Available online: <https://atlas.web.cern.ch/Atlas/GROUPS/PHYSICS/PUBNOTES/ATL-PHYS-PUB-2018-027> (accessed on 6 August 2021).
37. ATLAS sensitivity to dark matter produced in association with heavy quarks at the HL-LHC. Technical Report; All Figures Including Auxiliary Figures; CERN, Geneva, 2018. Available online: <https://atlas.web.cern.ch/Atlas/GROUPS/PHYSICS/PUBNOTES/ATL-PHYS-PUB-2018-036> (accessed on 6 August 2021).
38. CidVidal, X.; D’Onofrio, M.; Fox, P.J.; Torre, R.; Ulmer, K.A.; Aboubrahim, A.; Albert, A.; Alimena, J.; Allanach, B.C.; et al. Report from Working Group 3. *CERN Yellow Rep. Monogr.* **2019**, *7*, 585–865, doi:10.23731/CYRM-2019-007.585.
39. Branco, G.C.; Ferreira, P.M.; Lavoura, L.; Rebelo, M.N.; Sher, M.; Silva, J.P. Theory and phenomenology of two-Higgs-doublet models. *Phys. Rept.* **2012**, *516*, 1–102, doi:10.1016/j.physrep.2012.02.002.
40. Porod, W. SPheno, a program for calculating supersymmetric spectra, SUSY particle decays and SUSY particle production at e+e- colliders. *Comput. Phys. Commun.* **2003**, *153*, 275–315, doi:10.1016/S0010-4655(03)00222-4.
41. Porod, W.; Staub, F. SPheno 3.1: Extensions including flavour, CP-phases and models beyond the MSSM. *Comput. Phys. Commun.* **2012**, *183*, 2458–2469, doi:10.1016/j.cpc.2012.05.021.
42. Staub, F. SARAH. *arXiv* **2008**, arXiv:0806.0538.
43. Staub, F. From Superpotential to Model Files for FeynArts and CalcHep/CompHep. *Comput. Phys. Commun.* **2010**, *181*, 1077–1086, doi:10.1016/j.cpc.2010.01.011.
44. Staub, F. Automatic Calculation of supersymmetric Renormalization Group Equations and Self Energies. *Comput. Phys. Commun.* **2011**, *182*, 808–833, doi:10.1016/j.cpc.2010.11.030.
45. Staub, F. SARAH 3.2: Dirac Gauginos, UFO output, and more. *Comput. Phys. Commun.* **2013**, *184*, 1792–1809, doi:10.1016/j.cpc.2013.02.019.
46. Staub, F. SARAH 4: A tool for (not only SUSY) model builders. *Comput. Phys. Commun.* **2014**, *185*, 1773–1790, doi:10.1016/j.cpc.2014.02.018.
47. Altarelli, G.; Barbieri, R. Vacuum polarization effects of new physics on electroweak processes. *Phys. Lett.* **1991**, *B253*, 161–167, doi:10.1016/0370-2693(91)91378-9.
48. Peskin, M.E.; Takeuchi, T. A New constraint on a strongly interacting Higgs sector. *Phys. Rev. Lett.* **1990**, *65*, 964–967, doi:10.1103/PhysRevLett.65.964.
49. Peskin, M.E.; Takeuchi, T. Estimation of oblique electroweak corrections. *Phys. Rev.* **1992**, *D46*, 381–409, doi:10.1103/PhysRevD.46.381.
50. Baak, M.; Cúth, J.; Haller, J.; Hoecker, A.; Kogler, R.; Mönig, K.; Schott, M.; Stelzer, J. The global electroweak fit at NNLO and prospects for the LHC and ILC. *Eur. Phys. J.* **2014**, *C74*, 3046, doi:10.1140/epjc/s10052-014-3046-5.
51. GFitter: A Generic Fitter Project for HEP Model Testing. Available online: <http://project-gfitter.web.cern.ch/project-gfitter/> (accessed on 9 February 2019).
52. Haller, J.; Hoecker, A.; Kogler, R.; Mönig, K.; Peiffer, T.; Stelzer, J. Update of the global electroweak fit and constraints on two-Higgs-doublet models. *Eur. Phys. J.* **2018**, *C78*, 675, doi:10.1140/epjc/s10052-018-6131-3.
53. Arbey, A.; Mahmoudi, F.; Stal, O.; Stefaniak, T. Status of the Charged Higgs Boson in Two Higgs Doublet Models. *Eur. Phys. J.* **2018**, *C78*, 182, doi:10.1140/epjc/s10052-018-5651-1.
54. Misiak, M.; Rehman, A.; Steinhauser, M. Towards $\bar{B} \rightarrow X_s \gamma$ at the NNLO in QCD without interpolation in m_c . *J. High Energy Phys.* **2020**, *6*, 175, doi:10.1007/JHEP06(2020)175.
55. Misiak, M.; Asatrian, H.M.; Boughezal, R.; Czakon, M.; Ewerth, T.; Ferroglia, A.; Fiedler, P.; Gambino, P.; Greub, C.; Haisch, U.; et al. Updated NNLO QCD predictions for the weak radiative B-meson decays. *Phys. Rev. Lett.* **2015**, *114*, 221801, doi:10.1103/PhysRevLett.114.221801.
56. Misiak, M. (University of Warsaw, Warsaw, Poland). Personal communication, 2020.
57. The ATLAS, CMS and LHCb Collaborations. *Combination of the ATLAS, CMS and LHCb Results on the $B_{(s)}^0 \rightarrow \mu^+ \mu^-$ Decays*; Technical Report ATLAS-CONF-2020-049; CERN: Geneva, Switzerland, 2020.
58. Cheng, X.D.; Yang, Y.D.; Yuan, X.B. Revisiting $B_s \rightarrow \mu^+ \mu^-$ in the two-Higgs doublet models with Z_2 symmetry. *Eur. Phys. J.* **2016**, *C76*, 151, doi:10.1140/epjc/s10052-016-3930-2.
59. Beneke, M.; Bobeth, C.; Szafron, R. Power-enhanced leading-logarithmic QED corrections to $B_q \rightarrow \mu^+ \mu^-$. *J. High Energy Phys.* **2019**, *10*, 232, doi:10.1007/JHEP10(2019)232.
60. Amhis, Y.S.; Banerjee, S.w.; Ben-Haim, E.; Bernlocher, F.U.; Bona, M.; Bozek, A.; Bozzi, C.; Brodzicka, J.; Chrzaszcz, M.; Dingfelder, J.; et al. Averages of b-hadron, c-hadron, and τ -lepton properties as of 2018. *Eur. Phys. J.* **2021**, *C81*, 226, doi:10.1140/epjc/s10052-020-8156-7.
61. Lenz, A.; Nierste, U.; Charles, J.; Descotes-Genon, S.; Jantsch, A.; Kaufhold, C.; Lacker, H.; Monteil, S.; Niess, V.; T’Jampens, S. Anatomy of New Physics in $B - \bar{B}$ mixing. *Phys. Rev.* **2011**, *D83*, 036004, doi:10.1103/PhysRevD.83.036004.
62. Lenz, A.; Nierste, U. Numerical Updates of Lifetimes and Mixing Parameters of B Mesons. CKM unitarity triangle. In Proceedings of the 6th International Workshop, CKM 2010, Warwick, UK, 6–10 September 2010.
63. Nierste, U. (KIT Karlsruhe, Karlsruhe, Germany). Personal communication, 2020.
64. Aoki, S.; Aoki, Y.; Becirevic, D.; Blum, T.; Colangelo, G.; Collins, S.; Della Morte, M.; Dimopoulos, P.; Duerr, S.; Fukaya, H.; et al. FLAG Review 2019. *Eur. Phys. J.* **2020**, *C80*, 113, doi:10.1140/epjc/s10052-019-7354-7.

65. Dowdall, R.J.; Davies, C.T.H.; Horgan, R.R.; Lepage, G.P.; Monahan, C.J.; Shigemitsu, J.; Wingate, M. Neutral B-meson mixing from full lattice QCD at the physical point. *Phys. Rev.* **2019**, *D100*, 094508, doi:10.1103/PhysRevD.100.094508.
66. Zyla, P.A.; Barnett, P.A.; Beringer, J.; Dahl, O.; Dwyer, D.A.; Groom, D.E.; Lin, C.-J.; Lugovsky, K.S.; Pianori, E.; Robinson, D.J.; et al. Review of Particle Physics. *Prog. Theor. Exp. Phys.* **2020**, *2020*, 083C01. doi:10.1093/ptep/ptaa104.
67. Sirunyan, A.M.; Tumasyan, A.; Adam, W.; Ambrogio, F.; Asilar, E.; Bergauer, T.; Brandstetter, M.J.; Dragicevic, M.; Eroo, J.; Escalante Del Valle, A.; et al. Measurements of the Higgs boson width and anomalous HVV couplings from on-shell and off-shell production in the four-lepton final state. *Phys. Rev.* **2019**, *D99*, 112003, doi:10.1103/PhysRevD.99.112003.
68. Bechtle, P.; Brein, O.; Heinemeyer, S.; Weiglein, G.; Williams, K.E. HiggsBounds: Confronting Arbitrary Higgs Sectors with Exclusion Bounds from LEP and the Tevatron. *Comput. Phys. Commun.* **2010**, *181*, 138–167, doi:10.1016/j.cpc.2009.09.003.
69. Bechtle, P.; Brein, O.; Heinemeyer, S.; Weiglein, G.; Williams, K.E. HiggsBounds 2.0.0: Confronting Neutral and Charged Higgs Sector Predictions with Exclusion Bounds from LEP and the Tevatron. *Comput. Phys. Commun.* **2011**, *182*, 2605–2631, doi:10.1016/j.cpc.2011.07.015.
70. Bechtle, P.; Brein, O.; Heinemeyer, S.; Stal, O.; Stefaniak, T.; Weiglein, G.; Williams, K. Recent Developments in HiggsBounds and a Preview of HiggsSignals. *PoS* **2012**, *CHARGED2012*, 024. doi:10.22323/1.156.0024.
71. Bechtle, P.; Brein, O.; Heinemeyer, S.; Stål, O.; Stefaniak, T.; Weiglein, G.; Williams, K.E. HiggsBounds-4: Improved Tests of Extended Higgs Sectors against Exclusion Bounds from LEP, the Tevatron and the LHC. *Eur. Phys. J.* **2014**, *C74*, 2693, doi:10.1140/epjc/s10052-013-2693-2.
72. Bechtle, P.; Heinemeyer, S.; Stal, O.; Stefaniak, T.; Weiglein, G. Applying Exclusion Likelihoods from LHC Searches to Extended Higgs Sectors. *Eur. Phys. J.* **2015**, *C75*, 421, doi:10.1140/epjc/s10052-015-3650-z.
73. HiggsBounds and HiggsSignals. Available online: <https://higgsbounds.hepforge.org/> (accessed on 28 February 2019).
74. Bechtle, P.; Dercks, D.; Heinemeyer, S.; Klingl, T.; Stefaniak, T.; Weiglein, G.; Wittbrodt, J. HiggsBounds-5: Testing Higgs Sectors in the LHC 13 TeV Era. *Eur. Phys. J.* **2020**, *C80*, 1211, doi:10.1140/epjc/s10052-020-08557-9.
75. Stål, O.; Stefaniak, T. Constraining extended Higgs sectors with HiggsSignals. *PoS* **2013**, *EPS-HEP2013*, 314, doi:10.22323/1.180.0314.
76. Bechtle, P.; Heinemeyer, S.; Stål, O.; Stefaniak, T.; Weiglein, G. HiggsSignals: Confronting arbitrary Higgs sectors with measurements at the Tevatron and the LHC. *Eur. Phys. J.* **2014**, *C74*, 2711, doi:10.1140/epjc/s10052-013-2711-4.
77. Bechtle, P.; Heinemeyer, S.; Stål, O.; Stefaniak, T.; Weiglein, G. Probing the Standard Model with Higgs signal rates from the Tevatron, the LHC and a future ILC. *J. High Energy Phys.* **2014**, *11*, 039, doi:10.1007/JHEP11(2014)039.
78. Bechtle, P.; Heinemeyer, S.; Klingl, T.; Stefaniak, T.; Weiglein, G.; Wittbrodt, J. HiggsSignals-2: Probing new physics with precision Higgs measurements in the LHC 13 TeV era. *Eur. Phys. J.* **2021**, *C81*, 145, doi:10.1140/epjc/s10052-021-08942-y.
79. Alwall, J.; Herquet, M.; Maltoni, F.; Mattelaer, O.; Stelzer, T. MadGraph 5: Going Beyond. *J. High Energy Phys.* **2011**, *6*, 128, doi:10.1007/JHEP06(2011)128.
80. LHC-DMWG/model-repository. Available online: https://github.com/LHC-DMWG/model-repository/tree/master/models/Pseudoscalar_2HDM (accessed on 9 February 2019).
81. HEPData. Available online: <https://www.hepdata.net/record/ins1782373> (accessed on 3 July 2020).
82. Search for Dark Matter Produced in Association with a Single Top Quark in $\sqrt{s} = 13$ TeV pp Collisions with the ATLAS Detector. Available online: [https://atlas.web.cern.ch/Atlas/GROUPS/PHYSICS/PAPERS/EXOT-2018-43/\\$#Sauxstuff](https://atlas.web.cern.ch/Atlas/GROUPS/PHYSICS/PAPERS/EXOT-2018-43/$#Sauxstuff) (accessed on 17 November 2020).
83. Backovic, M.; Krämer, M.; Maltoni, F.; Martini, A.; Mawatari, K.; Pellen, M. Higher-order QCD predictions for dark matter production at the LHC in simplified models with s-channel mediators. *Eur. Phys. J.* **2015**, *C75*, 482, doi:10.1140/epjc/s10052-015-3700-6.
84. HEPData. Available online: <https://www.hepdata.net/record/ins1633591> (accessed on 9 February 2019).
85. Tumasyan, A. Search for new particles in events with energetic jets and large missing transverse momentum in proton-proton collisions at $\sqrt{s} = 13$ TeV. *JHEP* **2021**, *11*, 153, doi:10.1007/JHEP11(2021)153.
86. HEPData. Available online: <https://www.hepdata.net/record/ins1894408> (accessed on 2 September 2021).
87. Backovic, M.; Kong, K.; McCaskey, M. MadDM v.1.0: Computation of Dark Matter Relic Abundance Using MadGraph5. *Phys. Dark Univ.* **2014**, *5–6*, 18–28, doi:10.1016/j.dark.2014.04.001.
88. Backović, M.; Martini, A.; Mattelaer, O.; Kong, K.; Mohlabeng, G. Direct Detection of Dark Matter with MadDM v.2.0. *Phys. Dark Univ.* **2015**, *9–10*, 37–50, doi:10.1016/j.dark.2015.09.001.
89. Ambrogio, F.; Arina, C.; Backovic, M.; Heisig, J.; Maltoni, F.; Mantani, L.; Mattelaer, O.; Mohlabeng, G. MadDM v.3.0: A Comprehensive Tool for Dark Matter Studies. *Phys. Dark Univ.* **2019**, *24*, 100249, doi:10.1016/j.dark.2018.11.009.
90. Arcadi, G.; Lindner, M.; Queiroz, F.S.; Rodejohann, W.; Vogl, S. Pseudoscalar Mediators: A WIMP model at the Neutrino Floor. *J. Cosmol. Astropart. Phys.* **2018**, *1803*, 042, doi:10.1088/1475-7516/2018/03/042.
91. Bell, N.F.; Busoni, G.; Sanderson, I.W. Loop Effects in Direct Detection. *J. Cosmol. Astropart. Phys.* **2018**, *1808*, 017; Erratum in **2019**, *1901*, E01. doi:10.1088/1475-7516/2018/08/017.
92. Aghanim, N.; Akrami, Y.; Ashdown, M.; Aumont, J.; Baccigalupi, C.; Ballardini, M.; Banday, A.J.; Barreiro, R.B.; Bartolo, N.; Basak, S.; et al. Planck 2018 results. VI. Cosmological parameters. *Astron. Astrophys.* **2020**, *641*, A6; Erratum in **2021**, *652*, C4. doi:10.1051/0004-6361/201833910.

93. Aprile, E.; Aalbers, J.; Agostini, F.; Alfonsi, M.; Althueser, L.; Amaro, F.D.; Anthony, M.; Arneodo, F.; Baudis, L.; Bauermeister, B.; et al. Dark Matter Search Results from a One Ton-Year Exposure of XENON1T. *Phys. Rev. Lett.* **2018**, *121*, 111302, doi:10.1103/PhysRevLett.121.111302.
94. Belyaev, A.; Blandford, J.; Locke, D. PhenoData Database. Available online: <https://hepmdb.soton.ac.uk/phenodata> (accessed on 2 September 2019).
95. Eberhardt, O.; Martínez, A.P.; Pich, A. Global fits in the Aligned Two-Higgs-Doublet model. *J. High Energy Phys.* **2021**, *5*, 005, doi:10.1007/JHEP05(2021)005.
96. Enomoto, T.; Watanabe, R. Flavor constraints on the Two Higgs Doublet Models of Z_2 symmetric and aligned types. *J. High Energy Phys.* **2016**, *5*, 002, doi:10.1007/JHEP05(2016)002.
97. Sirunyan, A.M.; Tumasyan, A.; Adam, W.; Ambrogio, F.; Asilar, E.; Bergauer, T.; Brandstetter, J.; Dragicovic, M.; Eroo, J.; Escalante Del Valle, A.; et al. Combined measurements of Higgs boson couplings in proton–proton collisions at $\sqrt{s} = 13$ TeV. *Eur. Phys. J.* **2019**, *C79*, 421, doi:10.1140/epjc/s10052-019-6909-y.
98. Aad, G.; Abbott, B.; Abbott, D.C.; Abed Abud, A.; Abeling, K.; Abhayasinghe, D.K.; Abidi, S.H.; AbouZeid, O.S.; Abraham, N.L. Combined measurements of Higgs boson production and decay using up to 80 fb^{-1} of proton-proton collision data at $\sqrt{s} = 13$ TeV collected with the ATLAS experiment. *Phys. Rev.* **2020**, *D101*, 012002, doi:10.1103/PhysRevD.101.012002.
99. Kling, F.; Su, S.; Su, W. 2HDM Neutral Scalars under the LHC. *J. High Energy Phys.* **2020**, *6*, 163, doi:10.1007/JHEP06(2020)163.
100. Han, T.; Li, S.; Su, S.; Wu, Y. Comparative Studies of 2HDMs under the Higgs Boson Precision Measurements. *J. High Energy Phys.* **2021**, *1*, 045, doi:10.1007/JHEP01(2021)045.
101. The ATLAS Collaboration. *A Combination of Measurements of Higgs Boson Production and Decay Using up to 139 fb^{-1} of Proton–Proton Collision Data at $\sqrt{s} = 13$ TeV Collected with the ATLAS Experiment*; Technical Report ATLAS-CONF-2020-027; CERN: Geneva, Switzerland, 2020.
102. Aad, G.; Abbott, B.; Abbott, D.C.; Abed Abud, A.; Abeling, K.; Abhayasinghe, D.K.; Abidi, S.H.; AbouZeid, O.S.; Abraham, N.L.; Abramowicz, H.; et al. Search for heavy Higgs bosons decaying into two tau leptons with the ATLAS detector using pp collisions at $\sqrt{s} = 13$ TeV. *Phys. Rev. Lett.* **2020**, *125*, 051801, doi:10.1103/PhysRevLett.125.051801.
103. Aaboud, M.; Aad, G.; Abbott, B.; Abdinov, O.; Abeloos, B.; Abidi, S.H.; AbouZeid, O.S.; Abraham, N.L.; Abramowicz, H.; Abreu, H.; et al. Search for pair production of Higgs bosons in the $b\bar{b}b\bar{b}$ final state using proton-proton collisions at $\sqrt{s} = 13$ TeV with the ATLAS detector. *J. High Energy Phys.* **2019**, *1*, 030, doi:10.1007/JHEP01(2019)030.
104. Aaboud, M.; Aad, G.; Abbott, B.; Abdinov, O.; Abeloos, B.; Abidi, S.H.; AbouZeid, O.S.; Abraham, N.L.; Abramowicz, H.; Abreu, H.; et al. Search for a heavy Higgs boson decaying into a Z boson and another heavy Higgs boson in the $\ell\bar{\ell}b\bar{b}$ final state in pp collisions at $\sqrt{s} = 13$ TeV with the ATLAS detector. *Phys. Lett.* **2018**, *B783*, 392–414, doi:10.1016/j.physletb.2018.07.006.
105. The ATLAS Collaboration. *Search for Heavy Resonances Decaying into a Z Boson and a Higgs Boson in Final States with Leptons and b-Jets in 139 fb^{-1} of pp Collisions at $\sqrt{s} = 13 \text{ TeV}$ with the ATLAS Detector*; Technical Report; All Figures Including Auxiliary Figures; CERN: Geneva, Switzerland 2020; Available online: <https://atlas.web.cern.ch/Atlas/GROUPS/PHYSICS/CONFNOTES/ATLAS-CONF-2020-043> (accessed on 28 July 2020).
106. Chatrchyan, S.; Khachatryan, V.; Sirunyan, A.M.; Tumasyan, A.; Adam, W.; Bergauer, T.; Dragicovic, M.; Eroo, J.; Fabjan, C.; Friedl, M.; et al. Measurement of the Properties of a Higgs Boson in the Four-Lepton Final State. *Phys. Rev.* **2014**, *D89*, 092007, doi:10.1103/PhysRevD.89.092007.
107. Aad, G.; Abbott, B.; Abbott, D.C.; Abud, A.A.; Abeling, K.; Abhayasinghe, D.K.; Abidi, S.H.; AbouZeid, O.S.; Abraham, N.L.; Abramowicz, H.; et al. Search for a heavy Higgs boson decaying into a Z boson and another heavy Higgs boson in the $\ell\bar{\ell}b\bar{b}$ and $\ell\bar{\ell}WW$ final states in pp collisions at $\sqrt{s} = 13$ TeV with the ATLAS detector. *Eur. Phys. J.* **2021**, *C81*, 396, doi:10.1140/epjc/s10052-021-09117-5.
108. Kalinowski, J.; Kotlarski, W.; Robens, T.; Sokolowska, D.; Zarnecki, A.F. Exploring Inert Scalars at CLIC. *J. High Energy Phys.* **2019**, *7*, 053, doi:10.1007/JHEP07(2019)053.
109. de Blas, J. The CLIC Potential for New Physics. 2018. Available online: <https://e-publishing.cern.ch/index.php/CYRM/issue/view/71> (accessed on 28 July 2020). doi:10.23731/CYRM-2018-003.
110. Abi, B.; Albahri, T.; Al-Kilani, S.; Allspach, D.; Alonzi, L.P.; Anastasi, A.; Anisenkov, A.; Azfar, F.; Badgley, K.; Baessler, S.; et al. Measurement of the Positive Muon Anomalous Magnetic Moment to 0.46 ppm. *Phys. Rev. Lett.* **2021**, *126*, 141801, doi:10.1103/PhysRevLett.126.141801.
111. Cherchiglia, A.; Stoekinger, D.; Stoekinger-Kim, H. Muon $g-2$ in the 2HDM: maximum results and detailed phenomenology. *Phys. Rev.* **2018**, *D98*, 035001, doi:10.1103/PhysRevD.98.035001.
112. Ferreira, P.M.; Gonçalves, B.L.; Joaquim, F.R.; Sher, M. $(g-2)\mu$ in the 2HDM and slightly beyond: An updated view. *Phys. Rev. D* **2021**, *104*, 053008, doi:10.1103/PhysRevD.104.053008.
113. Cherchiglia, A.; Kneschke, P.; Stöckinger, D.; Stöckinger-Kim, H. The muon magnetic moment in the 2HDM: complete two-loop result. *J. High Energy Phys.* **2017**, *1*, 007; Erratum in **2021**, *10*, 242. doi:10.1007/JHEP10(2021)242.
114. Bennett, G.W.; Bousquet, B.; Brown, H.N.; Bunce, G.; Carey, R.M.; Cushman, P.; Danby, G.T.; Debevec, P.T.; Deile, M.; Deng, H.; et al. Final Report of the Muon E821 Anomalous Magnetic Moment Measurement at BNL. *Phys. Rev.* **2006**, *D73*, 072003, doi:10.1103/PhysRevD.73.072003.